

# Upgrade for Phase II of the GERDA Experiment

The GERDA collaboration<sup>a</sup>,

M. Agostini<sup>15</sup>, A.M. Bakalyarov<sup>13</sup>, M. Balata<sup>1</sup>, I. Barabanov<sup>11</sup>,  
L. Baudis<sup>19</sup>, C. Bauer<sup>7</sup>, E. Bellotti<sup>8,9</sup>, S. Belogurov<sup>12,11,b</sup>, S.T. Belyaev<sup>13,c</sup>,  
G. Benato<sup>19</sup>, A. Bettini<sup>16,17</sup>, L. Bezrukov<sup>11</sup>, T. Bode<sup>15</sup>, D. Borowicz<sup>5,d</sup>,  
V. Brudanin<sup>5</sup>, R. Brugnera<sup>16,17</sup>, A. Caldwell<sup>14</sup>, C. Cattadori<sup>9</sup>,  
A. Chernogorov<sup>12</sup>, V. D'Andrea<sup>1</sup>, E.V. Demidova<sup>12</sup>, N. Di Marco<sup>1</sup>,  
A. Domula<sup>4</sup>, E. Doroshkevich<sup>11</sup>, V. Egorov<sup>5</sup>, R. Falkenstein<sup>18</sup>,  
N. Frodyma<sup>3</sup>, A. Gangapshev<sup>11,7</sup>, A. Garfagnini<sup>16,17</sup>, P. Grabmayr<sup>18</sup>,  
V. Gurentsov<sup>11</sup>, K. Gusev<sup>5,13,15</sup>, J. Hakenmüller<sup>7</sup>, A. Hegai<sup>18</sup>, M. Heisel<sup>7</sup>,  
S. Hemmer<sup>16,17</sup>, R. Hiller<sup>19</sup>, W. Hofmann<sup>7</sup>, M. Hult<sup>6</sup>, L.V. Inzhechik<sup>11,e</sup>,  
L. Ioannucci<sup>1</sup>, J. Janicskó Csáthy<sup>15,f</sup>, J. Jochum<sup>18</sup>, M. Junker<sup>1</sup>,  
V. Kazalov<sup>11</sup>, Y. Kermaidic<sup>7</sup>, T. Kihm<sup>7</sup>, I.V. Kirpichnikov<sup>12</sup>, A. Kirsch<sup>7</sup>,  
A. Kish<sup>19</sup>, A. Klimenko<sup>7,5</sup>, R. Kneißl<sup>14</sup>, K.T. Knöpfle<sup>7</sup>, O. Kochetov<sup>5</sup>,  
V.N. Kornoukhov<sup>12,11</sup>, V.V. Kuzminov<sup>11</sup>, M. Laubenstein<sup>1</sup>, A. Lazzaro<sup>15</sup>,  
V.I. Lebedev<sup>13</sup>, B. Lehnert<sup>4,g</sup>, M. Lindner<sup>7</sup>, I. Lippi<sup>17</sup>, A. Lubashevskiy<sup>5</sup>,  
B. Lubsandorzhev<sup>11</sup>, G. Lutter<sup>6</sup>, C. Macolino<sup>1,h</sup>, B. Majorovits<sup>14</sup>,  
W. Maneschg<sup>7</sup>, E. Medinaceli<sup>16,17</sup>, M. Miloradovic<sup>19</sup>, R. Mingazheva<sup>19</sup>,  
M. Misiaszek<sup>3</sup>, P. Moseev<sup>11</sup>, I. Nemchenok<sup>5</sup>, S. Nisi<sup>1</sup>, K. Panas<sup>3</sup>,  
L. Pandola<sup>2</sup>, K. Pelczar<sup>1</sup>, A. Pullia<sup>10</sup>, C. Ransom<sup>19</sup>, S. Riboldi<sup>10</sup>,  
N. Rumyantseva<sup>5,13</sup>, C. Sada<sup>16,17</sup>, F. Salamida<sup>1,??</sup>, M. Salathe<sup>7</sup>,  
C. Schmitt<sup>18</sup>, B. Schneider<sup>4</sup>, S. Schönert<sup>15</sup>, J. Schreiner<sup>7</sup>, A-K. Schütz<sup>18</sup>,  
O. Schulz<sup>14</sup>, B. Schwingenheuer<sup>7</sup>, O. Selivanenko<sup>11</sup>, E. Shevchik<sup>5</sup>,  
M. Shirchenko<sup>5</sup>, H. Simgen<sup>7</sup>, A. Smolnikov<sup>7,5</sup>, L. Stanco<sup>17</sup>, L. Vanhoefer<sup>14</sup>,  
A.A. Vasenko<sup>12</sup>, A. Veresnikova<sup>11</sup>, K. von Sturm<sup>16,17</sup>, V. Wagner<sup>7</sup>,  
A. Wegmann<sup>7</sup>, T. Wester<sup>4</sup>, C. Wiesinger<sup>15</sup>, M. Wojcik<sup>3</sup>, E. Yanovich<sup>11</sup>,  
I. Zhitnikov<sup>5</sup>, S.V. Zhukov<sup>13</sup>, D. Zinatulina<sup>5</sup>, A.J. Zsigmond<sup>14</sup>, K. Zuber<sup>4</sup>,  
G. Zuzel<sup>3</sup>

<sup>1</sup>INFN Laboratori Nazionali del Gran Sasso and Gran Sasso Science Institute, Assergi, Italy

<sup>2</sup>INFN Laboratori Nazionali del Sud, Catania, Italy

<sup>3</sup>Institute of Physics, Jagiellonian University, Cracow, Poland

<sup>4</sup>Institut für Kern- und Teilchenphysik, Technische Universität Dresden, Dresden, Germany

<sup>5</sup>Joint Institute for Nuclear Research, Dubna, Russia

<sup>6</sup>European Commission, JRC-Geel, Geel, Belgium

<sup>7</sup>Max-Planck-Institut für Kernphysik, Heidelberg, Germany

<sup>8</sup>Dipartimento di Fisica, Università Milano Bicocca, Milano, Italy

<sup>9</sup>INFN Milano Bicocca, Milano, Italy

<sup>10</sup>Dipartimento di Fisica, Università degli Studi di Milano e INFN Milano, Milano, Italy

<sup>11</sup>Institute for Nuclear Research of the Russian Academy of Sciences, Moscow, Russia

<sup>12</sup>Institute for Theoretical and Experimental Physics, NRC “Kurchatov Institute”, Moscow, Russia

<sup>13</sup>National Research Centre “Kurchatov Institute”, Moscow, Russia

<sup>14</sup>Max-Planck-Institut für Physik, München, Germany

<sup>15</sup>Physik Department and Excellence Cluster Universe, Technische Universität München, München, Germany

<sup>16</sup>Dipartimento di Fisica e Astronomia dell'Università di Padova, Padova, Italy

<sup>17</sup>INFN Padova, Padova, Italy

<sup>18</sup>Physikalisches Institut, Eberhard Karls Universität Tübingen, Tübingen, Germany

<sup>19</sup>Physik Institut der Universität Zürich, Zürich, Switzerland

File: upgrade-p2-v5.tex, compiled: November 7, 2017

**Abstract** The GERDA collaboration is performing a sensitive search for neutrinoless double beta decay of  $^{76}\text{Ge}$  at the INFN Laboratori Nazionali del Gran Sasso, Italy. The upgrade of the GERDA experiment from Phase I to Phase II has been concluded in December 2015. The first Phase II data release shows that the goal to suppress the background by one order of magnitude compared to Phase I has been achieved. GERDA is thus the first experiment that will remain background-free up to its design exposure (100 kg·yr). It will reach thereby a half-life sensitivity of more than  $10^{26}$  yr within 3 years of data collection. This paper describes in detail the modifications and improvements of the experimental setup for Phase II and discusses the performance of individual detector components.

## 1 Introduction

Neutrinoless double beta ( $0\nu\beta\beta$ ) decay is a hypothetical lepton number violating process,  $(A,Z)\rightarrow(A,Z+2)+2e^-$ , where inside a nucleus two neutrons convert into two protons and two electrons. Its observation would establish the neutrino to be its own anti-particle (Majorana particle), provide access to the absolute mass scale of neutrinos, and support extensions of the Standard Model of particle physics which try to explain the dominance of baryonic matter over anti-matter in our universe [1]. Recent experiments have established the half-life of  $0\nu\beta\beta$  decay to be larger than  $10^{25}$  yr [2], and hence its detection requires the utmost suppression of any kind of background.

The GERmanium Detector Array (GERDA) collaboration searches at the INFN Laboratori Nazionali del Gran Sasso (LNGS) for  $0\nu\beta\beta$  decay of  $^{76}\text{Ge}$ ,  $^{76}\text{Ge}\rightarrow^{76}\text{Se}+2e^-$ . The GERDA experiment has been conceived in two phases. Here, a short overview of the experimental setup of Phase I which lasted from November 2011 until September 2013 is presented, while a detailed description has been given elsewhere [3].

<sup>a</sup>INFN Laboratori Nazionali del Gran Sasso, Italy.

*Correspondence*, email: gerda-eb@mpi-hd.mpg.de

<sup>b</sup>also at: NRNU MEPhI, Moscow, Russia

<sup>c</sup>deceased

<sup>d</sup>also at: The Henryk Niewodniczanski Institute of Nuclear Physics PAS, Krakow, Poland

<sup>e</sup>also at: Moscow Institute for Physics and Technology, Moscow, Russia

<sup>f</sup>present address: IKZ, Dresden, Germany

<sup>g</sup>present address: Carleton University, Ottawa, Canada

<sup>h</sup>present address: LAL, CNRS/IN2P3, Université Paris-Saclay, Orsay, France

<sup>i</sup>also at: Dipartimento di Scienze Fisiche e Chimiche, Università degli Studi di L'Aquila, L'Aquila, Italy

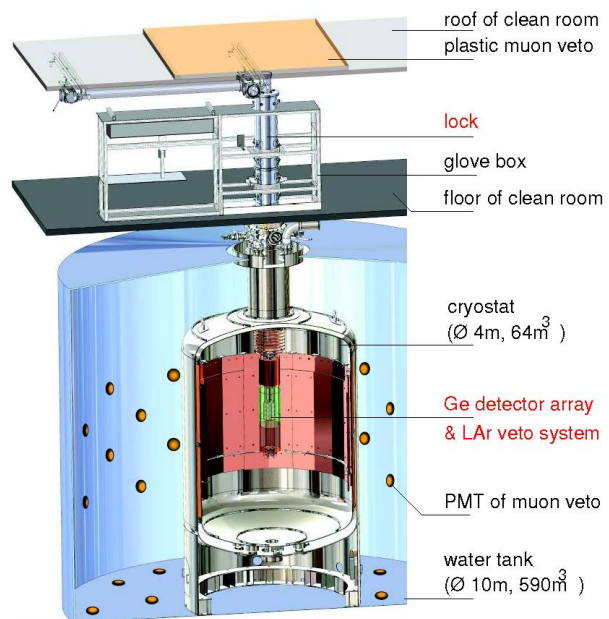


**Fig. 1** GERDA setup. The new Phase II components are labeled in red.

The GERDA experiment is located underground below a rock overburden of about 3500 m water equivalent that eliminates the hadronic component of cosmic ray showers and reduces the muon flux to  $\sim 1.25/(\text{m}^2\cdot\text{h})$ . GERDA uses high purity germanium (HPGe) detectors enriched in  $^{76}\text{Ge}$  which are arranged in strings within a cryostat filled with  $64\text{m}^3$  of liquid argon (quality 5.0), see Fig. 1. The liquid argon (LAr) acts both as cooling and shielding medium. The cryostat itself is enclosed by a large tank containing  $590\text{m}^3$  of ultra-pure water produced by the BOREXINO water plant [4]; the 2-3 m thick water layer serves both as additional passive shield as well as the medium for a Cherenkov veto system with 66 photomultiplier tubes (PMTs) against muons. A clean room on top of the cryostat and water tank houses a glove box and the lock for assembly and deployment of the Ge detectors.

The Phase 1 detector array, 4 strings in total, consisted of 8 enriched semi-coaxial Ge detectors with a total mass of 15.6 kg and 3 semi-coaxial Ge detectors from low-background natural material. The one string of natural Ge detectors was replaced in July 2012 by 5 Broad Energy Germanium (BEGe) detectors with a total mass of 3.6 kg; these diodes served as prototypes for Phase II.

The physics results of Phase I [6] were based on an exposure of 21.6 kg·yr. The energy scale was determined by (bi)weekly calibrations with  $^{228}\text{Th}$  sources. In the region of interest (ROI) around  $Q_{\beta\beta} = 2039$  keV, the interpolated exposure-averaged energy resolution of

the enriched semi-coaxial and BEGe detectors was determined to be 4.8(2) keV and 3.2(2) keV in terms of full-width-at-half-maximum (FWHM), respectively. A background index (BI) of about  $10^{-2}$  cts/(keV·kg·yr) was achieved, one order of magnitude lower than in the best previous  $0\nu\beta\beta$  decay searches with  $^{76}\text{Ge}$ . No signal was found for  $0\nu\beta\beta$  decay, and a new 90% confidence level (CL) limit of  $T_{1/2}^{0\nu} > 2.1 \cdot 10^{25}$  yr was derived (median sensitivity  $2.4 \cdot 10^{25}$  yr) that strongly disfavored a previous claim of observation [7]. Further Phase I results include a much improved half-life for  $2\nu\beta\beta$  decay of  $^{76}\text{Ge}$  and improved limits for Majoron  $\beta\beta$  decay modes [8], as well as  $2\nu\beta\beta$  decays of  $^{76}\text{Ge}$  into excited states of  $^{76}\text{Se}$  [9].

Phase II of GERDA was designed to improve the sensitivity on the half-life of  $0\nu\beta\beta$  decay by about one order of magnitude. At the end of Phase I GERDA had left the background-free regime<sup>1</sup> where sensitivity scales linearly with exposure  $\mathcal{E} = M \cdot t$ , the product of detector mass  $M$  and measurement period  $t$ , and entered the background i.e. statistical fluctuation limited scenario where it scales approximately with the square root of exposure divided by the background index BI and the energy resolution  $\Delta E$ ,  $\sqrt{(\mathcal{E}/(BI \cdot \Delta E))}$ . An efficient upgrade requires thus to re-enter the background-free regime, that means to not only increase exposure (detector mass) but also to reduce correspondingly the background (see Fig. 2). Improvements of the already excellent resolution are possible but limited to a factor of about 2 for the given technology. GERDA thus needs

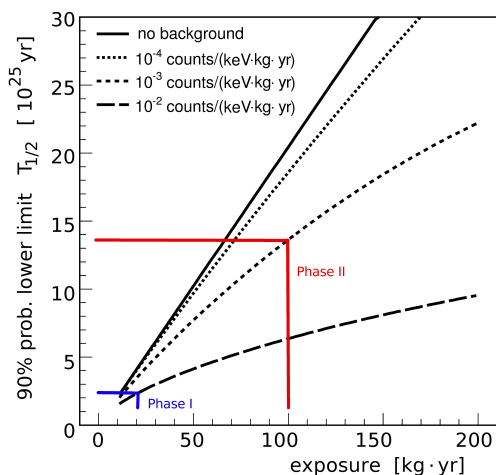


**Fig. 2** Estimated sensitivity of the GERDA experiment as a function of exposure for various background indices. The scenarios for GERDA Phase I and II are indicated [5].

<sup>1</sup>The background-free regime is effective if the background contribution is less than 1 in the energy region of interest ( $Q_{\beta\beta} \pm 0.5$  FWHM).

to achieve a BI of  $10^{-3}$  cts/(keV·kg·yr) in Phase II in order to reach the desired sensitivity beyond  $10^{26}$  yr at an exposure of about 100 kg·yr (see Fig. 2).

The analysis of the Phase I data showed that most background events were due to radioactive isotopes in materials close to the detectors [10]. The straightforward consequence was to further reduce material close to the detectors and/or to replace it by material of higher radiopurity. The major BI reduction had to come, however, from a largely improved discrimination of background events taking full advantage of their different event topology. While  $0\nu\beta\beta$  events normally deposit energy in a confined volume (a few  $\text{mm}^3$ ) of the detector, the background events can also deposit energy in the LAr around the detector, at the detector surface, or scatter at several locations in the detector. Events can thus be identified as background by coincident scintillation light in the LAr, by coincidences within the detector array and/or by the analysis of the signal pulse shape. GERDA has taken full advantage of all these options in Phase II: the additional batch of 20 kg of enriched Ge detectors consists of diodes of the novel BEGe type exhibiting superior pulse shape discrimination (PSD) [12] and energy resolution; a larger and more densely packed detector array exhibits enhanced efficiency for detector-detector (anti-)coincidences, and importantly, the LAr around the detector array has been instrumented for the readout of scintillation light creating thus an effective active LAr veto system. The efficacy of this approach has indeed been proven by the first results obtained with the upgraded GERDA experiment. Started in December 2015, the Phase II physics run reached in June 2016 the exposure of 10.8 kg·yr. These accumulated data have been already sufficient to demonstrate that the projected background level of  $10^{-3}$  cts/(keV·kg·yr) has been achieved and, to extract in combination with the Phase I data set a new lower limit for the  $0\nu\beta\beta$  decay half-life of  $^{76}\text{Ge}$  of  $> 5.3 \cdot 10^{25}$  yr at 90% CL [11].

The following sections describe the modifications of the GERDA experimental setup for Phase II including the new detector components and their performance. Section 2 presents an overview of the properties of the coaxial and BEGe detectors making up the Phase II detector array; it provides also details of the new mechanical mounts, cabling, electrical contacts and the cold electronic front end. A major part of this paper, Section 3, is devoted to the LAr veto system. Section 4 discusses the modifications of the infrastructure, in particular the new lock needed for the largely increased detector array and the LAr veto system. Section 5 summarizes the screening results for the newly introduced components. The performance of the individual sub-

systems and the background level achieved in Phase II until April 2017 are presented in Section 6. Conclusions are given in Section 7.

## 2 Germanium detectors

### 2.1 Characteristics of Phase II detectors

The GERDA Phase II detector array includes 7 strings, which carry 40 detectors in total. The detectors can be divided into three groups: the newly produced BEGe detectors, the semi-coaxial ANG and RG detectors, and the semi-coaxial GTF detectors [3]. The detectors of the first two groups are made of germanium enriched in  $^{76}\text{Ge}$  ( $^{\text{enr}}\text{BEGe}$ ,  $^{\text{enr}}\text{Coax}$ ), while those of the third group are made of germanium with natural isotopic abundance ( $^{\text{nat}}\text{Coax}$ ). The main properties of the individual detectors groups are discussed below, the properties of the individual detectors are listed in the Appendix (see Table 14).

#### 2.1.1 The semi-coaxial detectors

The 7 semi-coaxial  $^{76}\text{Ge}$  enriched detectors (ANG, RG), which originated from the former Heidelberg-Moscow and IGEX experiments, represented the core of GERDA Phase I [3]. In GERDA Phase II, they have again been included.

The  $^{76}\text{Ge}$  enrichment fractions of the ANG and RG detectors are in the range of 85.5 % to 88.3 %. All  $^{\text{enr}}\text{Coax}$  detectors have masses greater than 2 kg, except ANG1. The total mass is 15.578(7) kg. The applied bias voltages coincide nearly with those  $V_{\text{rec}}$  recommended by the manufacturer [13]. The  $^{76}\text{Ge}$  content of the 3 natural GTF detectors corresponds to the natural abundance of 7.8 %.

#### 2.1.2 The BEGe detectors

In order to increase the exposure (via increase of total detector mass) and to improve the background index (via an enhanced pulse shape performance), the GERDA collaboration opted for the production of 30 new detectors following the BEGe design of the company Canberra [14]. After extensive preparation, 30 detectors were delivered. Only one detector, GD02D, turned out to be rather a p-n junction than of p-type material, and thus suitable only for anti-coincidence studies in GERDA.

The 30  $^{\text{enr}}\text{BEGe}$  detectors have an enrichment fraction of 87.8 %. The diameters of the detectors range from 58.3(1) mm to 79.0(1) mm, and their heights from 22.9(3) to 35.3(1) mm. In 21 cases the detectors are

cylindric, in 9 cases they have a conical shape. The latter shape was tolerated in order to maximize the number of crystal slices that can be obtained from one single crystal ingot. The total mass is 20.024(30) kg. Herein, the  $\pm 1$  g error from weighing was assumed to be correlated for all detectors. Neglecting the detector GD02D, the total detector mass is reduced to 19.362(29) kg.

The average active volume fraction  $f_{\text{av}}$  and the total active mass  $M_{\text{av}}$  of all 29 fully operational GERDA Phase II BEGe detectors have been determined combining the full charge collection depth (FCCD) results from  $^{241}\text{Am}$  and  $^{133}\text{Ba}$  source measurements conducted in the HADES underground laboratory [15]. Moreover, an increase of the FCCD of 0.2 to 0.3 mm due to storage at room temperature over a period of nearly 3 years has been considered. All in all this led to:

$$f_{\text{av}} = 0.885_{-0.015}^{+0.016}(\text{uncorr}) \quad {}_{-0.003}^{+0.006}(\text{corr}) \quad (1)$$

$$M_{\text{av}} = 17.132_{-0.294}^{+0.315}(\text{uncorr}) \quad {}_{-0.063}^{+0.123}(\text{corr}) \text{ kg.} \quad (2)$$

Compared to the initial purified Ge powder used for crystal pulling, a crystal mass yield of 50.1 % and an active mass yield of 48.2 % were achieved (see Table 1). Considering that approximately 25 % of the kerf material could be recovered, the achieved total mass yield is high.

**Table 1** Crystal and active mass yield in % from enriched germanium to the final 30 BEGe detectors for GERDA Phase II. The mass transfer fractions are given relative to the original enriched  $\text{GeO}_2$  material (3rd column) and to the purified metallic Ge used for crystal growth (4th column).

| operation                             | germanium<br>(kg) | relative fraction |       |
|---------------------------------------|-------------------|-------------------|-------|
|                                       |                   | [%]               | [%]   |
| Ge in $\text{GeO}_2$ after enrichment | 37.5              | 100.0             | –     |
| purified Ge for crystal growth        | 35.5              | 94.1              | 100.0 |
| 30 produced diodes                    | 20.0              | 53.3              | 56.3  |
| 29 operational diodes                 | 19.4              | 51.7              | 54.6  |
| active mass of 29 diodes              | 17.1              | 45.6              | 48.2  |

The bias voltages applied on the detectors in GERDA coincide typically with the values  $V_{\text{rec}}$  recommended by the manufacturer (see Appendix Table 14). The collaboration, however, performed detailed voltage scans, in which depletion voltages and new operational voltages were determined which still guarantee uncompromised detector response. The new values are 600 V lower, on average. Indeed, GERDA operates in a few cases the detectors at these lower values, preventing thus unwanted high leakage currents or other instabilities.

The  $^{\text{enr}}\text{BEGe}$  detectors were characterized in vacuum cryostats within the HADES underground laboratory [15]. Note that these measurements were performed with ‘passivated’ detectors where the groove

between the  $p^+$  and  $n^+$  electrode is covered by an insulating silicon monoxide ('passivation') layer [14]. The energy resolution of all detectors turned out to be excellent. At the 1333 keV  $^{60}\text{Co}$   $\gamma$ -line the FWHM energy resolution is 1.72(7) keV, with best and worst values of 1.59 keV (GD89A) and 1.87 keV (GD79C). While a small dependence on the detector mass became visible, no dependence on the detector shape could be observed, i.e. cylindrical and conical ones have the same performance.

The pulse shape discrimination power was deduced from  $^{228}\text{Th}$  source measurements. For an event selection criterion keeping 90 % of signal-like events (double-escape peak events from the  $^{208}\text{Tl}$  line), the following survival probabilities for background-like event populations were found: the single-escape peak is reduced to (5-12) %, the full-energy peaks at 2615 and 1620 keV survive at (6-19) % and (9-19) %, respectively, and the Compton-events in the ROI are in the range of (32-48) %.

### 2.1.3 Electrical contacts

Aluminum bonding pads of 600 nm thickness have been evaporated on the  $p^+$  signal and  $n^+$  high-voltage electrodes of all Phase II detectors. The evaporation process had been developed in collaboration with the company Canberra and subsequently integrated together with the dedicated evaporation system into the manufacturer's production chain [16].

### 2.1.4 Activation by cosmic rays

Great attention has been paid to minimize the activation of the newly produced BEGe detectors by cosmic rays [14]. As of January 1 2017, we expect from cosmic activation in the 30 BEGes detectors (20.02 kg) about 24  $^{68}\text{Ge}$  nuclei and 300  $^{60}\text{Co}$  nuclei<sup>2</sup>; for comparison, the saturation activity is  $\sim 2300$   $^{68}\text{Ge}$  nuclei and  $\sim 9200$   $^{60}\text{Co}$  nuclei per kg germanium, respectively. Simulations show that during the year 2017 the decay of these nuclei will increase the background index before LAr veto and PSD by  $2.5 \cdot 10^{-4}$  cts/(keV·kg·yr) and  $0.34 \cdot 10^{-4}$  cts/(keV·kg·yr), respectively. For the semi-coaxial enriched detectors, the  $^{68}\text{Ge}$  activation has vanished due to their long underground storage; the  $^{60}\text{Co}$  contribution is about 1/3 of the expectation for the BEGe detectors.

<sup>2</sup>Activation rates at sea level vary from 1 to 13 and 1.6 to 6.7 nuclei/(kg·d) for  $^{68}\text{Ge}$  and  $^{60}\text{Co}$  nuclei, respectively. Here, we assume 5.8 and 3.3 nuclei/(kg·d) [14].

## 2.2 Detector Mount and Cabling

The GERDA Phase I background has been shown to originate predominantly from sources close to the Ge detectors. In addition, since the average mass ratio of BEGe to semi-coaxial detectors is about 1:3, further optimization of the detector mount for Phase II required to reduce the amount of construction materials and/or to improve their radiopurity. Fig. 3 shows the origi-

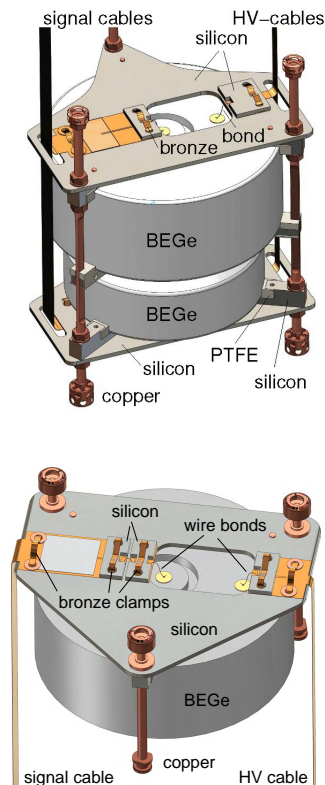


**Fig. 3** Alternative mounts for pairs of and single BEGe detectors, and their connection to the signal and high voltage (HV) flexible cables. The single detector module is viewed from bottom.

nal Phase II BEGe detector module which consists of 2 BEGe Ge diodes that are mounted back-to-back. The new design replaces the Phase I spring loaded contacts to the detector electrodes by 25  $\mu\text{m}$  diameter Al wire bonds. This allowed the substitution of a large part of the Phase I copper material (and PTFE) by monocrystalline silicon which is less strong but intrinsically extremely radio-pure (see Tables 2 and 8). The silicon plate serves both to define the position of the vertical copper bars which take the weight of the Ge detectors and to provide the substrate onto which signal and high voltage cables are attached with bronze clamps. The top and bottom of the copper bars carry bolts and nuts for the connection to another detector module.

**Table 2** Comparison of the masses  $m$  of construction materials for the Phase I and II detector holders, and of the masses  $m'$  normalized to 1 kg of detector mass assuming an average mass of 0.67 kg for single BEGe and 2.4 kg for semi-coaxial detectors.

| Material | Phase I (coaxial) |             | Phase II (BEGe) |             |
|----------|-------------------|-------------|-----------------|-------------|
|          | $m$ (g)           | $m'$ (g/kg) | $m$ (g)         | $m'$ (g/kg) |
| Cu       | 84                | 35.0        | 13              | 19.4        |
| Si       | 1                 | 0.4         | 20              | 29.9        |
| PTFE     | 7                 | 2.9         | 1               | 1.5         |
| CuSn6    | -                 | -           | 0.5             | 0.75        |
| total    | 92                | 38.3        | 34.5            | 51.55       |

Another advantage of the new holder is that the detector mounting procedure becomes easier and safer than in Phase I, since all mounting steps except bonding are being done without touching the diode. Thus the possibility to scratch the very sensitive  $p^+$  contact is minimized. Some detectors have been mounted and dismantled in their Phase II holders several times without any deterioration of their performance. Bonding also solved the previous problems of irreproducible HV contact quality.

During commissioning for Phase II, so far unknown problems with detector biasing and leakage currents showed up that were highly correlated with the orientation of BEGe detectors such that detectors with the groove pointing upwards, the ‘top’ detectors in the mount, were much more affected than the ‘bottom’ detectors with the groove pointing downwards. In Phase I all detectors had been indeed mounted with the groove pointing downwards. The problem could be attributed to microscopic particulates which had fallen into the groove during the mounting procedure or during operation in the LAr. Hence, the concept of mounting pairs of BEGe detectors was given up, and single BEGe detectors were mounted individually like the semi-coaxial detectors avoiding grooves pointing upwards (see Fig. 3, bottom). By the start of the Phase II physics run, all problematic BEGe pair assemblies and also the newly deployed detectors received the new holders which virtually eliminated the previous problems. It is planned to replace the mount of the 6 remaining BEGe pair assemblies in a forthcoming maintenance break.

The low-mass Phase II detector mount with its silicon plate has no tolerance against crack-producing stress, thus requires the detector assembly to be kept in a jig until finally deployed in the detector string. The rather compact jig is made from stainless steel and thoroughly cleaned in order to avoid contamination of the detector module. Fig. 4 shows a jig and detector module within a glove box, flushed with nitrogen, in front of

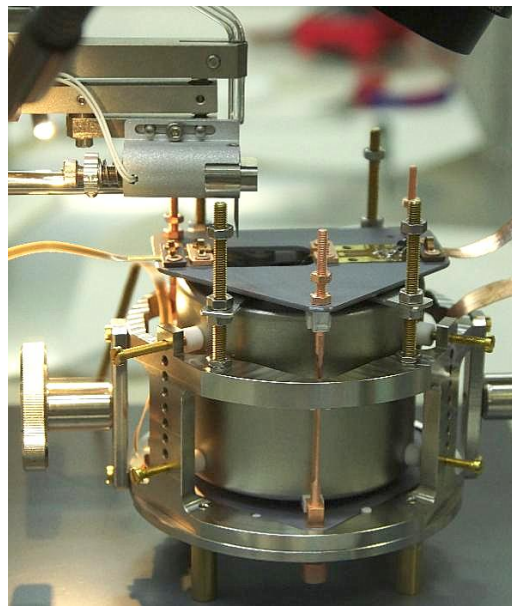


**Fig. 4** A detector module with two BEGe detectors within its jig. The top plate of the jig has been removed to provide full access for the deep-access bonder.

a deep-access bonder ready for connecting the flexible cables with the signal and HV contact of the top BEGe detector. After turning the jig for bonding the second detector, jig and module are stored in their dedicated vacuum container until deployment.

After mounting and bonding, each detector was tested for leakage current in the GERDA Germanium Detector Laboratory (GDL) which is also located underground at LNGS. All detectors that passed this test were integrated in the GERDA setup. However, about half of the diodes showed again high leakage currents already in the GDL test bench. They were dismantled from their holders and sent to Canberra for reprocessing and, in some cases, passivation. On return they were mounted again in the holders, tested in GDL and added to the GERDA setup at the final stage of integration.

### 2.3 Ge detector readout

The Ge detectors are read out with custom-produced preamplifiers called ‘CC3’. Fig. 5 shows the schematic of this cryogenic, low radioactivity, 4-channel charge sensitive amplifier [17,18]. It is a continuous resistor reset amplifier, made of two amplifying stages based on commercial CMOS operational amplifiers. Miniaturized SMD components and Ta capacitors, mostly in 0402 size, are chosen to minimize the radioactivity of the circuit (Fig. 6). The input stage is the BF862 JFET from NPX. The CC3 circuit has a sensitivity of

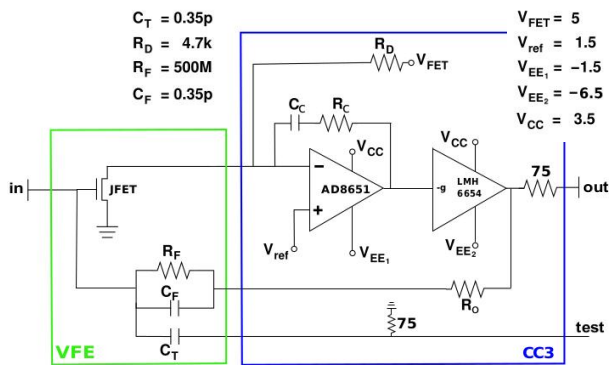


**Fig. 5** Schematic of one channel of the CC3 Ge readout circuit. The green frame shows the very front end (JFET, feedback resistor and capacitor), the blue frame shows the following stages.

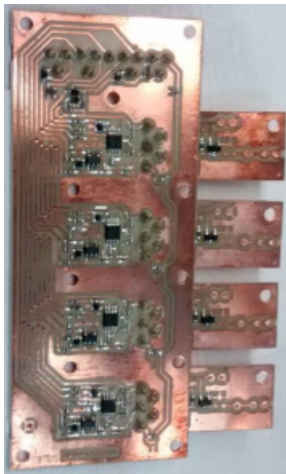


**Fig. 6** Photo of the CC3 Ge 4-channel readout circuit. Each circuit serves 4 channels. The very front end components (see Fig. 5) are located on the 4 small PCBs which are connected with low activity pin-contacts to the main board; this allows us to replace individually for each channel the components of the very front end, and in particular the rather sensitive JFET.

$\sim 150$  mV/MeV, a dynamic range of  $\sim 15$  MeV, a rise-time (10%-90%) of  $< 100$  ns,  $< 70$  mW/ch power consumption, and an intrinsic noise of  $\sim 0.8$  keV Ge-equivalent.

The Ge readout electrode is connected to the JFET-PCB by a flexible flat cable (FFC), made from Pyralux<sup>®</sup> or Cufion<sup>®</sup>. This allows for a detachable contact between the detector and the main front end board, without any glueing or soldering at the detector level, hence minimizing the activity close to the detectors while maximizing the contact reliability. Two different FFCs are adopted for the signal and HV contact: the HV FFCs are made from 10 mils Cufion<sup>®</sup>, or 3 mils Pyralux<sup>®</sup>,

the signal FFCs from 3 mils Cufion<sup>®</sup> or Pyralux<sup>®</sup>. For all FFCs the Cu trace is 2 mm wide and 18  $\mu$ m thick.

## 2.4 The seven detector strings

Fig. 7 shows the Ge detector array together with the electronic front end boards on top in about 30 cm distance. The height of the array is 40 cm, its diameter is about 30 cm. There are 7 strings with 40 detectors in

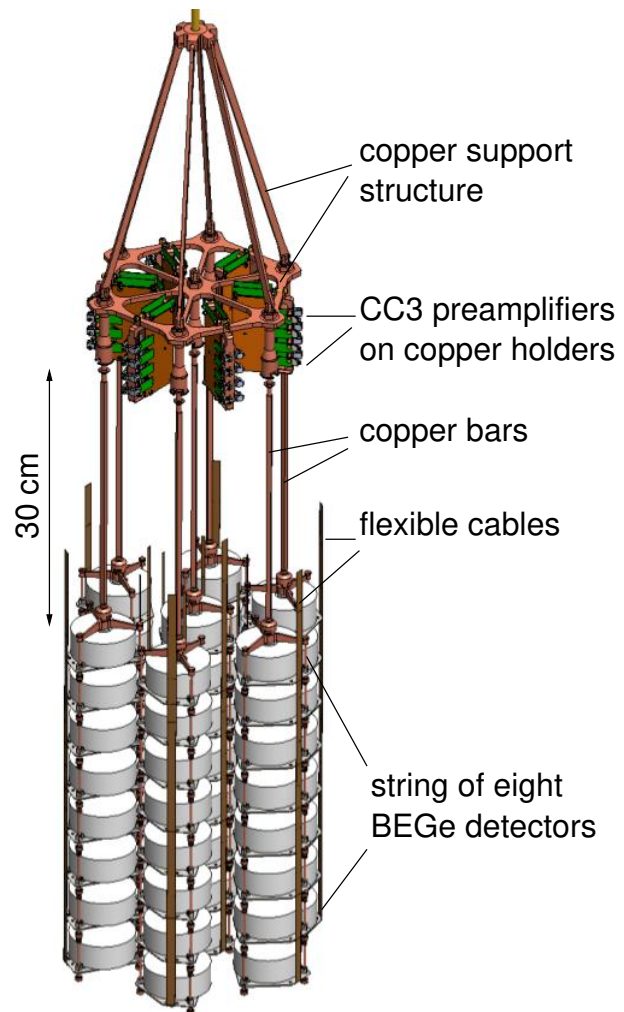


**Fig. 7** Arrangement of the seven detector strings with preamplifiers.

total. Six strings consist either of 8 BEGe or 3 semi-coaxial (enriched or natural) detectors. One string is a mixture of semi-coaxial and BEGe detectors. A photo of the detector array is shown in Fig. 31 (see Appendix).

Further figures in the Appendix show the array from the top including the location of the calibration sources as well as the inner boundary of the LAr veto system

(Fig. 32) and the detailed arrangement of all detectors (Fig. 33). Detectors marked with blue are passivated. It should be noted that, contrary to Phase I experience, no leakage current increase has been found for neither passivated nor non-passivated diodes after one year of operation (see Section 6 and Fig. 20).

### 2.5 The mini-shrouds for mitigating $^{42}\text{K}$ background

The background due to  $^{42}\text{Ar}$  is prominent in GERDA.  $^{42}\text{Ar}$  decays into  $^{42}\text{K}$ , which is a  $\beta$  emitter with an endpoint energy of 3.5 MeV. A copper cylinder, called ‘mini-shroud’ (MS), placed around the detectors was used for mitigation of  $^{42}\text{K}$  background in Phase I [3]. The MS screens the electric field of the detector and creates a mechanical barrier which prevents the collection of  $^{42}\text{K}$  ions on the detector surface. The volume from which  $^{42}\text{K}$  collection takes place becomes much smaller and thus the level of  $^{42}\text{K}$  background decreases. However, the copper MS cannot be used in GERDA Phase II since the LAr scintillation veto is implemented for the suppression of various backgrounds. Scintillation light generated inside the copper MS would not be visible by the LAr instrumentation and the efficiency of the LAr veto system would be considerably reduced. Another reason for the development of a new MS is the higher demands on radiopurity which would not have been met by the copper MS of Phase I.

That is why for Phase II a new MS made from ultra-pure nylon was developed [19]. A photo of the detector array with each string enclosed by its individual transparent MS is shown in Fig. 31 of the Appendix. Such a nylon MS does not screen the electric field of the detector like a copper one, but serves just as a barrier that stops the drift of  $^{42}\text{K}$  ions towards the detectors. The nylon films were provided by Princeton University. They were fabricated for the BOREXINO internal balloon [20]. The thickness of the films is 125  $\mu\text{m}$ . Similar to other plastics materials, nylon is almost opaque for the deep ultraviolet radiation generated in LAr. Hence it is covered on both sides with a wavelength shifter (WLS) based on tetra-phenyl-butadiene (TPB), that shifts the 128 nm scintillation light to wavelengths of about 450 nm, suitable for transport through the nylon and detection by the LAr veto system.

The investigation and development of the background suppression methods were done at the low-background test facility LARGE [21] in GDL. It was demonstrated that the nylon MS is robust enough to be deployed into the cryogenic liquid and that it does not deteriorate the LAr scintillation veto performance. By reducing the collection of  $^{42}\text{K}$  atoms at the surface of the Ge detector,

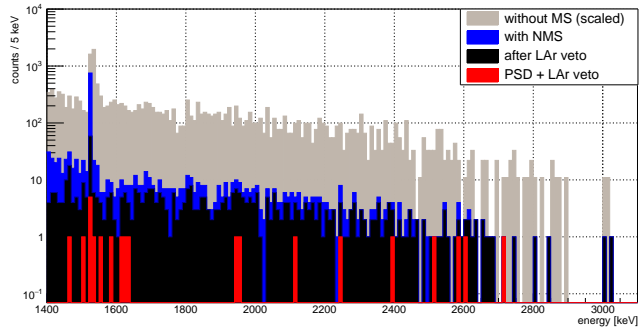


**Fig. 8** Suppression of the events from  $^{42}\text{Ar}$  decays by the nylon mini-shroud (NMS), LAr veto and PSD: the grey area shows the scaled spectrum from a measurement with a bare BEGe detector without NMS, ‘blue’ the measurement with NMS, ‘black’ the events surviving the LAr veto cut, and ‘red’ the remaining events after both the LAr veto and PSD cuts [19].

and by combining the PSD technique with the scintillation veto, it was possible to decrease the  $^{42}\text{K}$  background by more than a factor of  $10^3$  (see Fig. 8).

### 3 LAr veto system

The liquid argon veto system (LAr veto) of GERDA is a detector system devised to detect argon scintillation light in the vicinity of the Ge detector array. It evolved from studies of scintillation light detection in LAr with 8” PMTs in the low-background facility LARGE [21] and silicon photomultipliers (SiPMs) coupled to wave length shifting fibers for increasing light detection efficiency [22]. The goal is to reject those types of background events in the Ge detectors that simultaneously deposit energy in the surrounding LAr, and hence generate scintillation. These background types mainly include  $\gamma$ -ray background from Ra and Th decays in solid materials inside and around the detectors. But also other types of background can successfully be rejected, such as muons or decays from  $^{42}\text{Ar}/^{42}\text{K}$ . The concept of a LAr anti-coincidence veto has been proven in LARGE where suppression factors of up to a few times  $10^3$  were achieved depending on the background type and source distance towards the Ge detectors [21].

The LAr light instrumentation in GERDA is conceived as a hybrid system comprising PMTs and WLS fibers with SiPM readout. It is designed to be a retractable unit that can be deployed together with the Ge detector array into the cryostat through the lock system. The elaborated mounting scheme of the veto system is described in the next section. The lock system constrains the veto’s geometry to a lengthy cylindrical shape with a diameter of  $\sim 0.50$  m and a total height



of  $\sim 2.6$  m. A (CAD) technical drawing depicting the complete LAr veto system is shown in Fig. 9.

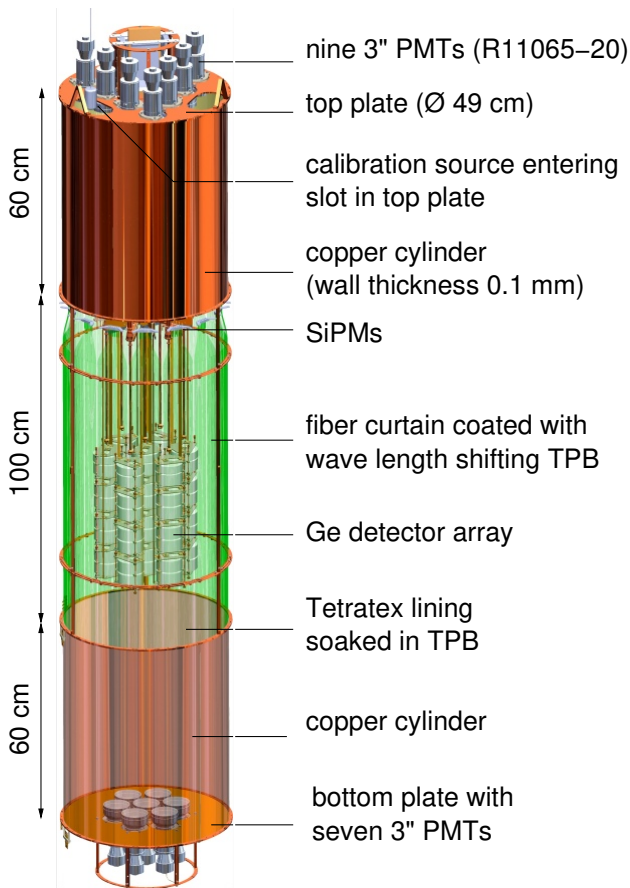


**Fig. 9** The Ge detector array enclosed by the LAr veto system.

### 3.1 PMT system

The PMT light readout system measures the scintillation light around the detector array with nine PMTs from the top and seven PMTs from the bottom. The 3" PMTs are installed on copper plates at the two ends of the cylindrical LAr volume facing inwards (see Figs. 10 and 11). These end plates are separated from the central fiber section by copper shrouds of 60 cm height. The copper shrouds consist of 100  $\mu$ m thick copper foils which carry laser-welded flanges at both ends for the connection to the PMT plates and the fiber section. They are lined with Tetratex<sup>®</sup> PTFE foil of 254  $\mu$ m thickness from the inside. The Tetratex<sup>®</sup> foil is impregnated with TPB, and thereby serves as a WLS of the scintillation and diffuse reflector of the shifted light.

The foil has been thoroughly tested for mechanical and optical stability of the WLS [23].

The cabling of the bottom PMTs runs along the outside of the LAr veto system. The bottom shroud can be easily detached from the central fiber unit within the glove box. For this purpose custom made low-radioactivity cable plugs for the bottom PMTs were placed on the connecting flange (see Fig. 12).

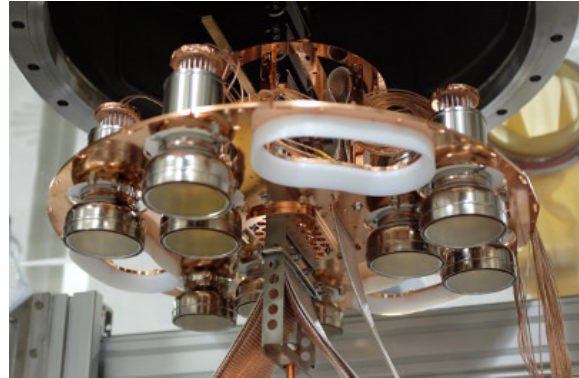


**Fig. 10** Top PMT plate with 9 PMTs and three longitudinal slots with PTFE guides for the deployment of the calibration sources.



**Fig. 11** Bottom PMT plate with 7 PMTs and copper cylinder. Plate and cylinder are covered by wavelength shifting Tetratex<sup>®</sup> foil soaked in TPB [23].

The PMTs are of type Hamamatsu R11065-20 Mod. They have a bi-alkali photocathode that reaches a quantum efficiency of about 40% at the wavelength of 420 nm. Typically a peak-to-valley ratio of about four is achieved for single photoelectrons. To enable direct detection of scintillation the photocathodes are coated with a 1-4  $\mu$ m thick layer of WLS, TPB (10% by mass) embedded in polystyrene (90%). In various test series it was

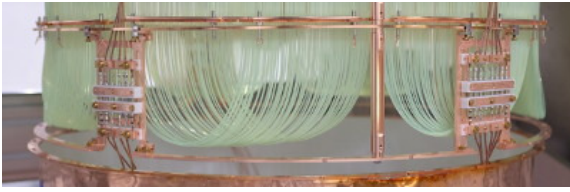


**Fig. 12** PMT cable plugs custom made from copper and PTFE allow to separate the bottom LAr veto segment from the central fiber part.

found that the first generation of R11065 PMTs was unstable under cryogenic conditions. However, in cooperation with the manufacturer it was possible to receive the current modified and improved version: each of the PMTs has been continuously operated for at least six weeks in a LAr test stand prior to the deployment in GERDA, and has been operated stably in GERDA since the start of Phase II more than one year ago (see Section 6).

The voltage dividers are designed for negative bias and high signal quality. The electrical power consumption is kept low at about 20 mW to prevent the argon from boiling. For further protection against discharges due to argon gas bubbles the PCB is potted into epoxy resin and a copper pot (see Fig. 13). Custom made SAMI RG178 coaxial cables are used for both signal and bias voltage inside the GERDA lock and cryostat.

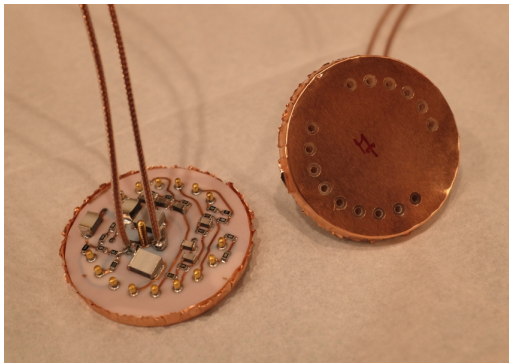


**Fig. 13** Voltage divider potted into epoxy resin.

The PMT signals are amplified outside of the lock by custom made shapers and split into two branches; one output leads to a FADC for digitization, and a second branch is used to independently monitor the count rates: the signals are fed into a custom made scaler device that applies a threshold of  $\sim 20\%$  photoelectron amplitude to count hits and store the rate in a database. The GERDA Slow Control has access to this database and invokes an immediate automatic safety ramp down of a PMT's bias voltage in case its rate ex-

ceeds a limit of 20 kHz. The bias power supply is the same CAEN SY1527 system as used for the Cherenkov veto PMTs [3]. High voltage filters are mounted at the feedthroughs to the GERDA lock to reduce electronic pickup noise on the bias power.

The gain of the PMTs is calibrated to  $(2-3) \cdot 10^6$  with bias voltages in the range from -1300 V to -1550 V. At these settings the peak-to-valley ratio reaches its best values of 3.5 to 4, which is relevant to identify hits above baseline noise at a low threshold. The gain is constantly monitored and found to be stable throughout the operation in GERDA (see Section 6).

### 3.2 The fiber-SiPM system



**Fig. 14** The fiber curtain: height  $\sim 1$  m, diameter  $\sim 0.5$  m, 405 fibers read out on both ends by 90 SiPMs.



**Fig. 15** Fiber holder produced with wire erosion. Note the pattern of diagonally aligned square holes. One holder covers an angular range of  $23.5^\circ$ .

The middle section of the LAr veto setup (Fig. 14) consists of a curtain ( $\sim 50\%$  coverage) of WLS fibers which are read out with SiPMs. Note that its field of view is limited by the copper radon shroud<sup>3</sup> at diameter 0.75 m.

### 3.2.1 Fiber curtain

The design goal of the fiber detector was to achieve the largest possible coverage with light detectors while using the minimum amount of material hence minimizing the radioactivity in the vicinity of the Ge detectors.

The BCF-91A multicladd fibers from Saint-Gobain with a cross section of  $1 \times 1 \text{ mm}^2$  were chosen. The square cross section is needed for the highest possible trapping efficiency and the absorption spectrum of the BCF-91A fiber matches well the emission spectrum of the TPB. The surface of the fibers is coated with TPB by vacuum deposition.

The fibers are supported by a lightweight copper frame that also carries the weight of the bottom PMT section of the setup.

The arrangement of the square fibers is such that their diagonal is tangential to the circular flanges maximizing their surface turned towards the enclosed volume. The fibers are held in place by copper holders as the one seen in Fig. 15. These holders bundle 54 fibers in one unit which are connected to six  $3 \times 3 \text{ mm}^2$  SiPMs.

At the bottom part of the fiber shroud the fibers are bent around and fed through the neighboring copper holder (see Fig. 14) such that two pairs of copper holders form a double module. Every single fiber is about 1.8 m long and both of its ends are instrumented with SiPMs at the top of the cylinder.

The total amount of fibers is about 730 m. This corresponds to a mass of about 765 g. The total surface is about  $2.9 \text{ m}^2$  half of which is facing inwards the enclosed volume.

<sup>3</sup> The radon shroud separates a central volume of about 3 m height and 0.75 m diameter from the remaining volume of the cryostat in order to prevent that radon, emanating e.g. from the walls of the vessel, may be transported by convection close to the detector array [3].

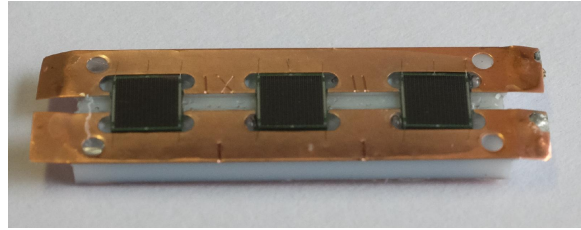


**Fig. 16** Custom packaging of three  $3 \times 3 \text{ mm}^2$  SiPMs on a Cuflon<sup>®</sup> holder.

### 3.2.2 SiPMs

For possible use in GERDA the radioactivity of commercial SiPMs is a big concern because of the substrate that is either ceramic or ordinary glass fiber PCB material. On the other hand the purity of the silicon wafers the chips are made of is expected to be very high. To have the radiopurity issue under control it was decided to pack the SiPMs ourselves. Therefore the  $3 \times 3 \text{ mm}^2$  SiPMs were purchased in die from Ketek GmbH.

The packaging consists of a Cuflon<sup>®</sup> PCB with square holes machined into it for the SiPM chips. Such a holder with SiPMs already implanted is shown in Fig. 16. Each holder has place for three SiPMs. The top copper layer of the PCB material is divided into two strips during the milling to form the two contacts of the SiPM array. The SiPMs are placed in the holder and bonded to the copper stripes. Then the holder is covered with a thin layer of transparent epoxy glue (Polytec EP601).

Each array was tested first at room temperature, then in liquid nitrogen (LN). The arrays that passed the first test were assembled in double arrays of six SiPMs and tested again in LN. Only fully functional SiPM arrays with low dark rate ( $< 1 \text{ Hz/mm}^2$  at about 2.7 V overvoltage in LN) were accepted for deployment in GERDA.

Six SiPMs are connected in parallel to one  $50 \Omega$  cable in the cable chain. There is no active or passive electronic component in the LAr. The total cable length from the SiPMs to the amplifier input is about 20 m.

The strongly temperature dependent quenching resistors of the SiPMs cause very long pixel recharge times in the range of microseconds when the SiPMs are submersed in LAr. In addition, the capacity of the large array and the cable reduces the peak amplitude of the signal significantly. The slow and small amplitude signals suggest the use of charge sensitive amplifiers.

Fig. 17 shows the readout circuit schematics. Each group of three SiPMs corresponds to a unit shown in Fig. 16. The transmission line in Fig. 17 stands for the 20 m cable mentioned above. The potentiometer regulates the bias voltage of the SiPMs which is connected

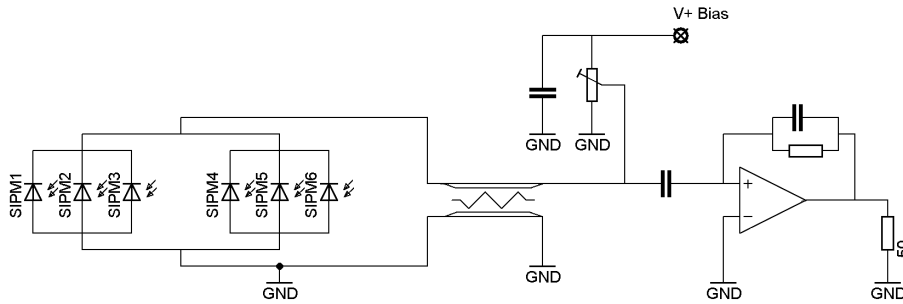


**Fig. 17** Circuit diagram of the SiPM readout. Only one channel is shown with six SiPMs in parallel which corresponds to an array of 54 mm<sup>2</sup>. The cable separating the SiPMs and the amplifier is about 20 m long. The charge sensitive amplifier is a Cremat-112.

to the core of the coaxial cable. The signal is decoupled with a 100 nF capacitor and connected to the charge sensitive amplifier (CR112 from Cremat). The bias circuit and the charge amplifier are mounted in a custom-made NIM module.

### 3.3 Data acquisition and analysis

The same FADC system (SIS 3301 Struck) used for the Ge detectors [3] records the pulse shapes of the 16 PMT and 15 SiPM channels and saves them for off-line analysis. The PMT traces are digitized with 100 MS/s and for each channel a trace of 12  $\mu$ s length is saved to disk. The resolution of the SiPM traces is reduced to 80 ns to save disk space but traces of 120  $\mu$ s length are recorded. All LAr channels are read out together with the Ge channels if at least one Ge detector has an energy deposition above 100 keV. Fig. 18 shows the traces of a representative background event that has been triggered by a Ge detector and that has produced in addition signals in the PMTs and SiPMs of the LAr veto system. PMT hits are reconstructed in the offline analysis following the procedure described in [24]. First, the baseline is determined using an iterative method from [25]. Then a leading edge trigger with a threshold of 3 baseline standard deviations is applied to identify up to fifteen hits per trace. Amplitude and charge of each hit are computed. No quality cuts or signal filtering is applied. The trigger positions are converted into time differences relative to the first trigger found in the Ge detector traces. Trigger positions and amplitudes are subsequently used together with hits from the SiPM to test the LAr veto condition.

SiPM hits in the recorded traces are identified with a trigger finding algorithm based on the trapezoidal filter. The moving window deconvolution is applied twice on the recorded traces. In the first step the decay time of the amplifier is deconvoluted (50  $\mu$ s) and in the second

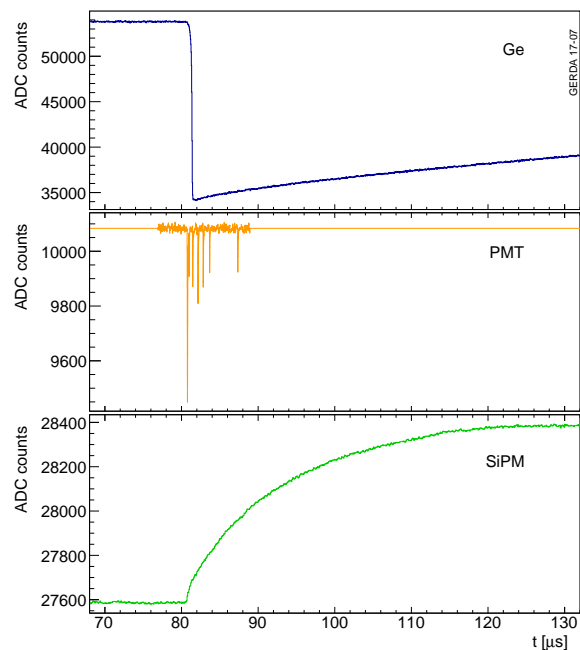


**Fig. 18** Sample traces of an event with signals in a Ge detector and the LAr veto system. On top the trace of the Ge detector that triggered the event; a PMT trace in the middle - the fast component of the scintillation light is followed by several smaller pulses from the triplet component; at bottom one of the SiPMs traces with the expected slower signal (see Subsection 3.2).

step the RC constant of the SiPM given by the quenching resistor times pixel capacity is removed. To determine the trigger time a trigger finding algorithm [24] is employed on the resulting waveform, and the amplitude of the pulses is read after a fixed delay following the trigger.

The algorithms were implemented in the GELATIO framework [26] which is used to process GERDA data. Each event is characterized by the calibrated energy deposited in the Ge diode, a data quality flag, the classification as signal or background event from the PSD

analysis, and veto flags from the muon veto and LAr veto systems.

#### 4 Upgrade of infrastructure

The break after the end of the Phase I run was used for both maintenance and upgrade work. After more than 3 years of operation the water tank was emptied. Selected welds and surfaces of both cryostat and water tank were inspected. No corrosion problems were observed, and the system safety of the pressure equipment was certified by a notified body. With the Phase I lock dismantled, a  $^{228}\text{Th}$  calibration source of 20 kBq was recovered that dropped by accident during Phase I to the bottom of the cryostat. While it did not affect the Phase I background index, its presence would have not been tolerable in Phase II. For this recovery the bottom of the radon shroud had to be cut out. Both actions were performed with remotely controlled tools in the LAr-filled and hermetically closed cryostat.

##### 4.1 Clean room upgrade

In order to improve the temperature stability within the clean room, the ventilation system was upgraded. An additional pump was installed that regulates the cooling water supply for the GERDA clean room ventilation system according to the needs. Flux sensors have been installed to strategic cold water tubes, allowing for real time monitoring of the cooling water throughput. These measures have led to an increase of temperature stability inside the clean room. While in Phase I the stability was about  $\pm 0.7^\circ\text{C}$  it could be now stabilized to  $\pm 0.2^\circ\text{C}$ . Additional temperature sensors have been installed to the body of the lock system. These show that temperature fluctuations of the experimental volume itself are smaller than  $\pm 0.1^\circ\text{C}$ . This improvement is relevant for the long term stability of the ohmic resistance of the readout cables.

##### 4.2 Muon veto system

The muon veto system [27] was slightly upgraded. For the replacement of the lock the plastic muon veto system had to be removed from the roof of the clean room. After reinstallation, a broken amplifier of the plastic veto was replaced.

During the inspection of the cryostat the water tank was empty and thus a refurbishment of the PMTs of the muon veto was possible. Being accessible without scaffolding, two of four broken PMTs could be replaced

by spare ones. At the beginning of Phase II, in total still 3 out of 66 Cherenkov PMTs were not working, 4 more failed during data collection. The plastic panels on the roof of the clean room (see Fig. 1) are working satisfactorily.

##### 4.3 Lock system

Keeping the same functional principle, the Phase II lock replaces the Phase I twin lock system by a single-arm lock with enlarged diameter (550 mm) and height (2682 mm). This allows us to deploy both the 7 string detector array and the complete assembly of the LAr veto instrumentation (see Fig. 19). Both detector sys-

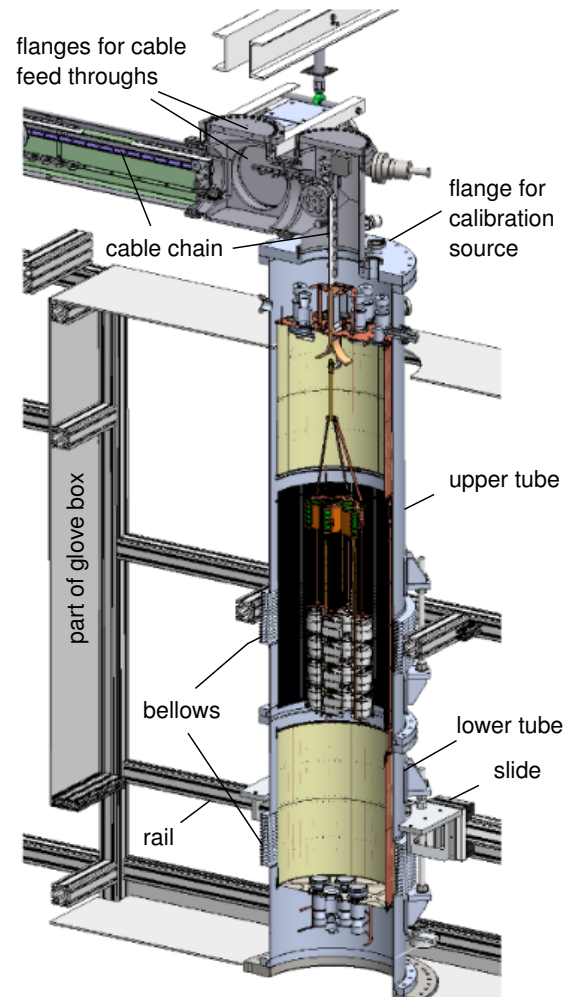


**Fig. 19** Vertical part of the Phase II lock with the Ge detector array and the LAr veto system in retracted position. Both upper and lower tube are enclosed by a glove box. The lower tube can be laterally moved such that the resulting gap allows the installation and service of both the Ge detector array and the LAr veto system.

tems are suspended from a chain which allows us to lower them by  $\sim 6$  m down to the center of the cryostat. Like in Phase I, the suspension chain also serves for guiding the cables.

#### 4.3.1 Functionality of lock

Two stainless steel tubes constitute the lock volume, an upper one of 1.75 m height, and a lower one of 0.93 m height. They mount vertically directly on the DN630 shutter which separates the cryostat's volume from atmosphere. Bellows and set-screws allow us to vary the length of both tubes by  $\pm 5$  cm. The lock is opened by sliding the lower tube horizontally to the side after its two flanges have been detached. The resulting gap allows to introduce the three segments of the LAr veto system successively into the lock. The top PMT plate represents the interface between cable chain and the upper copper shroud; it is permanently installed in the lock resting just by its weight on a keyed index plate which is attached at the end of the cable chain. The position of the top PMT plate can be locked by three bolts at the upper end of the top tube; thus the cable chain (and the Ge detector array) can be moved independently downward. In standard operation, when only the Ge detector array has to be serviced, the top and middle segments of the LAr veto system are thus retained in the upper tube of the lock while its bottom segment is moved together with the lower tube to the side.

All handling is done from the outside of the glove box via various appropriately positioned glove ports.

#### 4.3.2 Cables

The coaxial cables deployed inside the lock are custom produced to minimize both the total radioactivity and the outgassing of nitrogen and radon in the lock and in the LAr. In fact, nitrogen impurities are powerful LAr scintillation light quenchers and Rn progenies can cause an increase of background. 240 pieces of 12 m long coaxial cables have been deployed to connect the lock feedthroughs for signal, power supplies and HV to the front end circuits, Ge detectors, and the SiPMs and PMTs of the LAr veto system. Each Ge front end circuit (see Fig. 6) requires nine coaxial cables: four for the circuit power supply, one for the pulser, and four for the amplifier outputs. The cabling serves 11 front end circuits, 4 channels each plus spares. Three different cable types are deployed: RG179 for the Ge high voltage, RG178 50 Ohm for the SiPMs and PMTs bias and readout, and 75 Ohm coaxial cables for the signal outputs of the Ge charge sensitive preamplifiers. Table 3

**Table 3** List and characteristics of the coaxial cables in the 5 cable bands deployed in the GERDA Phase II cable chain.

|                            | RG178    | RG179         | 75 $\Omega$     |
|----------------------------|----------|---------------|-----------------|
| purpose                    | LAr veto | Ge HV         | Ge signal       |
| band:no of cables          | V:48     | I:35<br>II:35 | III:61<br>IV:61 |
| AWG                        | 30       | 30            | 33              |
| conductor                  | Cu       | Cu            | Cu              |
| dielectric                 | PFA      | PFA           | PFA             |
| $\emptyset$ [mm]           | 1.8      | 2.55          | 1.4             |
| impedance [ $\Omega$ ]     | 50       | 75            | 75              |
| attenuation [db/100m]      | 95       | 68            | 95              |
| capacity [pF]              | 95       | 64            | 70              |
| weight [g/m]               | 7        | 14            | 4               |
| resistivity [ $\Omega$ /m] | 0.37     | 0.37          | 1.5             |

shows the list of cables and their specifications. The constituent materials have been chosen to obey cryogenics specifications and minimize space occupancy, radioactivity and outgassing rates. For the HV cables, the dielectric strength of the insulator is relevant. The perfluoroalkoxy alkane (PFA) polymer material has been chosen because of its high dielectric strength. All the cables have been custom produced by SAMI<sup>4</sup>: both central and shielding conductor braids are in bare copper, and the dielectric and jacket material PFA has not been colored to preserve radiopurity, Rn emanation and minimize cable outgassing.

The cable outgassing has been measured both in vacuum tests and by chromatography on a RG179 sample of 100 m: thanks to high quality materials a total outgassing of  $10^{-6}$  mbar $\cdot\ell$ /s was achieved after 24 hours of pumping. The measurements were performed at 40°C, 100°C, and 150°C. Only at 100°C and 150°C, a few peaks of organic and fluor-organic compounds, octane and butane decafluoro-butane, showed up at few minutes arrival times. No peaks corresponding to known NIST Library nitrogen or nitrogen compounds were observed.

For deployment in the cable chain, the 240 cables have been woven in five cable bands of 95 mm width (see Table 3). Weaving was done with weaving machines at a commercial company<sup>5</sup>. Special care was taken to properly clean the cables and the PTFE thread prior to weaving. All parts of the weaving machine the cables got in touch with during the weaving process were disassembled and properly cleaned using ultrapure isopropanol and water. After weaving, the cable bands were once more cleaned, dried and packed under clean room conditions.

<sup>4</sup>SAMI Conduttori Elettrici Speciali, Via Venezia snc, 20060 Liscate (MI)

<sup>5</sup>PD Cable Systems, <http://www.pdcablesystems.de/index.html>

### 4.3.3 Cable chain

The cable chain and its supporting mechanics are designed to deploy a total mass of up to 60 kg. Made from stainless steel of 1.5 mm thickness, its cross section (102 mm width  $\times$  20 mm height, with a usable height of 12 mm) is enlarged by a factor of 7.5 relative to Phase I in order to accommodate the cable bands for the array and LAr veto system. A 1 m long piece of the cable chain has been used for stress tests applying a force up to 4.95 kN, corresponding to a test load on the pulley of  $\sim$ 200 kg. There was no sign of critical deformation.

When retracted, the cable chain is held inside a horizontal 3.9 m long DN250 tube by a pulley that runs along the length of the tube guided by a linear bearing. The cable chain is deflected around this pulley by  $180^\circ$  and above the cryostat neck by  $90^\circ$  vertically downwards. The pulley is connected to a metal band at the far side from the cryostat neck that can be rolled up on a winch. By unrolling the metal band the pulley moves towards the cryostat neck and the array suspended to the cable chain can be lowered into the cryostat (see Fig. 10 in Ref. [3]). At the far end from the cryostat a cross is connected to the horizontal tube with two CF flanges. These contain the feedthrough for the motor axle moving the suspension system as well as the vacuum and gas ports. On the close end to the cryostat two crosses with three CF250 flanges each are connected that carry all the signal and HV feedthroughs including the HV filters.

For movement of the array a stepper motor EC60 with gear GP81 and encoder provided by MAXON<sup>6</sup> is used. A magnetofluid rotational feedthrough with 20 mm axle provided by VacSol<sup>7</sup> is used for transmission of the motor movement onto the winch that is moving the cable chain, hence, the Ge detector array and LAr veto system.

### 4.3.4 PLC system

A new PLC system based on a Simatic S7-300 for the control of the array movements via the stepper motor, operation of the DN630 shutter between cryostat and lock system, pumps and LED control has been built. The system has been designed to maximize safety during operation via interlocks. Two redundant induction sensors on each side of the pulley system serve as end switches allowing a calibration of the system in the up and down position. The position of the array is obtained independently by the stepper position of the motor and

a measuring tape with holes. In case a significant deviation of position measurements is determined, the PLC stops movement of the array.

### 4.3.5 Fabrication and commissioning

All parts of the internals of the lock system were specially selected and screened for radioactivity using low background HPGe detectors and/or for radon emanation prior to mounting (see Section 5). The tubes have been designed and tested according to the European pressure vessel code.

The horizontal part of the Phase II lock system has been fully assembled under clean room ISO 5 conditions. All parts were cleaned in an ultrasonic bath inside a wet bench using ultra-pure water and isopropanol prior to mounting. After final mounting dry tests under clean room conditions were performed to verify mechanical precision and reproducibility of the positioning of test loads. Torsion of the cable chain leads to a reproducible rotation of the load of  $\sim(10\pm 2)^\circ$  when fully lowered.

Once mounted at LNGS on top of the GERDA cryostat the system was tested for vacuum leaks. None could be found at the level of  $10^{-8}$  mbar $\cdot\ell$ /s.

Before opening the DN630 shutter between lock and LAr cryostat, the system has been (and is) conditioned over 12 hours by several pumping cycles in order to ensure a low enough outgassing rate from cables and other parts of the internal mechanical components.

## 4.4 Calibration system

The well-proven Phase I calibration system [28] has been integrated into the Phase II lock system. New sources were produced for Phase II and characterized [29]. The three individual calibration units are mounted on the top flange of the lock. Their geometrical arrangement on a mounting circle of 380 mm diameter and an angular distance of  $120^\circ$  is such (Appendix Fig. 32) that each source, when lowered, just fits into the space between the cylinder of the LAr veto system and two neighboring outer strings of the detector array; thereby the sources enter the inner volume of the LAr veto system by three slots in the top PMT plate (see Fig. 10). A modification of the source holders, the insulation of the Ta absorber from the stainless steel band [28], prevents a previously observed HV instability in several Ge detectors.

Individual gate valves allow the units to be decoupled from the cryostat such that the respective calibration sources can be exchanged. Besides the standard

<sup>6</sup>maxon motor ag, <http://www.maxonmotor.ch>

<sup>7</sup>VacSol GmbH, <http://www.vacsol.com>

$^{228}\text{Th}$  source of low neutron emission [29], available sources include  $^{226}\text{Ra}$  and  $^{56}\text{Co}$ .

## 5 Material screening results

Compared to Phase I the amount of material deployed close to the detectors has increased in Phase II, and hence the constraints for the radiopurity of the respective materials have become even more restrictive. State-of-the-art screening techniques have been used again to verify the desired radiopurity. The available screening facilities have been discussed earlier in some detail [3]. They include Ge  $\gamma$  ray spectrometers in the underground laboratories at MPI-K Heidelberg, HADES (IRMM) in Belgium, and LNGS, Italy. Screening with Inductively Coupled Plasma Mass spectrometers (ICPMS) has been performed at LNGS and at INR RAS, Moscow. Radon emanation measurements were done with both the ultra-low background proportional counters developed originally at MPI-K Heidelberg for the Gallex experiment, and with the (less sensitive) permanently installed  $^{222}\text{Rn}$  electrostatic counter at GERDA.

In the following Subsections the uncertainties are given as  $\pm 1$  standard deviations and the limits are quoted at 68% CL.

### 5.1 Radon emanation inside the lock

$^{222}\text{Rn}$  emanated inside the lock may be dissolved in the LAr and contribute to the background. Hence the selection of low-emanating construction materials is crucial. All non-metal materials mounted inside the lock have been qualified by Rn emanation measurements prior to assembly. Additionally, all components located close to the detector array have been screened using HPGe detectors. Like in Phase I all flanges of the lock are sealed with metal gasket against atmosphere when possible. Else Kalrez O-rings were chosen whose low emanation rate had been established in Phase I [3].

The measured Rn emanation of the woven coaxial cables bands is given in Table 4. The total emanation rate expected from all cables is lower than 4.0 mBq. This is consistent with the total  $^{226}\text{Ra}$  activity from the woven cable bands obtained from HPGe screening (see Table 6) of  $\sim 10$  mBq, considering the fact that only a fraction of the  $^{222}\text{Rn}$  resulting from the decays of  $^{226}\text{Ra}$  does actually emanate from the cables.

Radon emanation measurements of the fully equipped lock system showed rates below the tolerable level. A saturation activity of  $(12.5 \pm 5)$  mBq was measured that has to be compared to  $(55 \pm 3.5)$  mBq from the cryostat alone.

**Table 4** Results from Radon emanation measurements of the woven cable bands (see Table 3).

| Band                    | activity [ $\mu\text{Bq}/\text{m}$ ] |
|-------------------------|--------------------------------------|
| 48 $\times$ RG178       | <266                                 |
| 35 $\times$ RG179       | <19                                  |
| 61 $\times$ 75 $\Omega$ | $12 \pm 2$                           |

### 5.2 Nylon mini-shrouds

The radioactive purity of the coated nylon films was checked by ICPMS measurements at LNGS [31]. Results of the measurements are shown in Table 5. Differences

**Table 5** Radioactive impurities of the components of one nylon mini-shroud (MS) from ICPMS measurements. Uncertainties are estimated to be about 30%.

| Component    | U<br>[ppt]         | Th<br>[ppt]        | K<br>[ppb]         | mass<br>[g] |
|--------------|--------------------|--------------------|--------------------|-------------|
| TPB          | 10                 | 9                  | 65                 |             |
| polystyrene  | <5                 | 10                 | 100                |             |
| glue         | <10                | <10                | 900                |             |
| nylon        | <10                | <15                | -                  | 27.6        |
| nylon coated | 11                 | 18                 | <25                |             |
| nylon glued  | 38                 | 39                 | 1200               |             |
| MS finished  | 6.1 $\mu\text{Bq}$ | 2.6 $\mu\text{Bq}$ | 242 $\mu\text{Bq}$ | 28.1        |

in radiopurity of similar samples indicated that surface contaminations play a big role; so it is important to prepare and keep foils in a clean condition. Coating of the nylon foils was performed in a clean room by brushing; this allows to deposit a small amount of WLS with a good enough coverage. The deposited WLS was determined by weighing the nylon before and after coating. A typical mass of the coating was about 0.3 mg/cm<sup>2</sup> for the nylon film coated from both sides.

To assess if the radiopurity level is acceptable, a detailed simulation of the nylon MS in the GERDA Phase II setup was performed [32]. The expected contribution of all mini-shrouds to the background index is about  $5 \cdot 10^{-4}$  cts/(keV·kg·yr) before LAr veto and PSD cuts, and two orders of magnitude lower after these cuts.

### 5.3 Coaxial Cables

Table 6 compares the length-specific activities of the coaxial cables deployed in the lock in Phase I and II. In Phase II, the high voltage cables (RG179) are factors of about 15 to 25 better in  $^{226}\text{Ra}$  and  $^{228}\text{Th}$ , and a factor of 50 better in  $^{40}\text{K}$  than in Phase I (TR11.18kV); compared to the standard production SAMI cables, they



**Table 6** The length-specific activities of the custom coaxial cables deployed in GERDA Phase II compared to the standard cables used in Phase I. All screening has been done with Ge  $\gamma$  spectrometers. Phase II cables were woven in bands (see Table 3).

| Cable     | $^{226}\text{Ra}$    | $^{228}\text{Th}$ | $^{40}\text{K}$ | $^{60}\text{Co}$ | $^{137}\text{Cs}$ | $^{108\text{m}}\text{Ag}$ | $^{110\text{m}}\text{Ag}$ |
|-----------|----------------------|-------------------|-----------------|------------------|-------------------|---------------------------|---------------------------|
|           | ( $\mu\text{Bq/m}$ ) |                   |                 |                  |                   |                           |                           |
| Phase I:  |                      |                   |                 |                  |                   |                           |                           |
| RG178     | $11 \pm 3$           | $13 \pm 5$        | 680             | $< 0.4$          | -                 | $13 \pm 2$                | $8 \pm 1$                 |
| TR11.18kV | 134                  | 96                | 3700            | -                | n.a.              | n.a.                      | n.a.                      |
| HABIA50   | $< 5$                | $3 \pm 2$         | 1200            | $< 1$            | -                 | $2 \pm 1$                 | $4 \pm 2$                 |
| Phase II: |                      |                   |                 |                  |                   |                           |                           |
| 75 Ohm    | $5 \pm 1$            | $5 \pm 1$         | $190 \pm 30$    | $< 1$            | $3 \pm 1$         | -                         | -                         |
| RG178     | $4 \pm 1$            | $< 5$             | $81 \pm 16$     | $< 2$            | -                 | -                         | -                         |
| RG179     | $< 5$                | $6 \pm 2$         | $74 \pm 15$     | $< 2$            | -                 | -                         | -                         |

**Table 7** The activity of the GERDA front-end cables and PCBs in Phase I and II. The Phase II front-end PCBs have been screened fully populated while the Phase I samples had no contact pins yet. The values of the Phase I readout / HV ‘cable’, a high-purity copper wire within a PTFE tube, refer to its insulation.

|                                    | Mass<br>(g) | $^{226}\text{Ra}$     | $^{228}\text{Th}$ | $^{40}\text{K}$ | $^{60}\text{Co}$ | $^{137}\text{Cs}$ |
|------------------------------------|-------------|-----------------------|-------------------|-----------------|------------------|-------------------|
|                                    |             | ( $\mu\text{Bq/pc}$ ) |                   |                 |                  |                   |
| Phase I:                           |             |                       |                   |                 |                  |                   |
| readout / HV ‘cable’ (1m)          | 4.28        | $4.7 \pm 0.9$         | $< 3.3$           | $34 \pm 9$      | -                | $< 1.5$           |
| 3-ch front end PCB w/o pins        | 5.2         | $290 \pm 100$         | $140 \pm 60$      | $1900 \pm 700$  | $< 56$           | $< 42$            |
| Phase II:                          |             |                       |                   |                 |                  |                   |
| Pyralux <sup>®</sup> 3 mil (80 cm) | 0.4         | $3 \pm 1$             | $4 \pm 1$         | $34 \pm 15$     | $< 0.55$         | $< 1.9$           |
| Cuflon <sup>®</sup> 3 mil (51 cm)  | 0.5         | $25 \pm 5$            | $< 11$            | $120 \pm 60$    | $< 9.2$          | $< 5.5$           |
| Cuflon <sup>®</sup> 10 mil (51 cm) | 2.7         | $21 \pm 6$            | $< 15$            | $300 \pm 80$    | $< 9.2$          | $< 6.5$           |
| 4-ch front end PCB                 | 17          | $230 \pm 30$          | $70 \pm 40$       | $1300 \pm 400$  | $< 27$           | $< 67$            |

are better by factors of about 20 to 30 in  $^{226}\text{Ra}$  and  $^{228}\text{Th}$  and  $^{40}\text{K}$ . The  $^{108\text{m}}\text{Ag}$  and  $^{110\text{m}}\text{Ag}$  isotopes are not present in the Phase II cables due to the bare copper choice for the conductor.

#### 5.4 Electronic front-end

Table 7 reports the measured activities of the FE devices. Compared to Phase I, the new FE circuits and contacts exhibit a significantly lower contamination, which is reduced for  $^{226}\text{Ra}$  and  $^{228}\text{Th}$  by a factor of 1.5 and 30 per channel, respectively. For a BI of  $10^{-3}$  cts/(keV·kg·yr) before LAr veto and PSD cuts, Monte Carlo (MC) simulations predict maximum allowed activities of 2 mBq and 0.5 mBq, respectively, if the electronics boards are mounted 30 cm above the top detectors. The total activity of the 10 boards amounts to 2.3(3) mBq and 0.7(4) mBq for  $^{226}\text{Ra}$  and  $^{228}\text{Th}$ , respectively, being thus close to the radiopurity limit.

For the front-end cables the corresponding limits are  $0.5 \mu\text{Bq/cm}$  for  $^{226}\text{Ra}$  and  $0.04 \mu\text{Bq/cm}$  for  $^{228}\text{Th}$ . The activity of the Pyralux<sup>®</sup> cables is well below the limit for  $^{226}\text{Ra}$  and almost meets the limit for  $^{228}\text{Th}$ . The

Cuflon<sup>®</sup> cables just meet the limit for  $^{226}\text{Ra}$  and miss it for  $^{228}\text{Th}$  by about a factor of 10. With 60% of the deployed front-end cables being of the Cuflon<sup>®</sup> type this excess reduces to a factor of  $\sim 4$ ; this is still tolerable since the LAr veto alone suppresses the  $^{228}\text{Th}$  induced background by about a factor of 100 (see Section 6).

#### 5.5 Detector holders

Table 8 compares the radiopurity of Phase I and Phase II detector holders. The substitution of copper by silicon mounting material results in significantly reduced  $^{228}\text{Th}$  and  $^{226}\text{Ra}$  activities. The corresponding contribution to the BI is less than  $3 \cdot 10^{-5}$  cts/(keV·kg·yr) according to simulations before LAr veto and PSD cuts.

#### 5.6 LAr veto system

The radiopurity of the components of the LAr veto system is critical since they add a large amount of new material close to the detector array. The activities of

**Table 8** Comparison of the radiopurity of the Phase I and II detector holders (for masses of construction materials see Table 2). Specific activities from neutron activation analysis (NAA) [30] and ICPMS assume secular equilibrium. The background contribution BI at  $Q_{\beta\beta}$  is estimated after anti-coincidences but before LAr veto and PSD.

| Material  | method         | specific activity   |                   |                 | total activity    |                   |                 | background index   |                   |
|-----------|----------------|---------------------|-------------------|-----------------|-------------------|-------------------|-----------------|--|-------------------|
|           |                | $^{228}\text{Th}$   | $^{226}\text{Ra}$ | $^{40}\text{K}$ | $^{228}\text{Th}$ | $^{226}\text{Ra}$ | $^{40}\text{K}$ | $^{208}\text{Tl}$  | $^{214}\text{Bi}$ |
|           |                | $(\mu\text{Bq/kg})$ |                   |                 | $(\mu\text{Bq})$  |                   |                 | $(10^{-6}\text{cts}/(\text{keV}\cdot\text{kg}\cdot\text{yr}))$ |                   |
| Phase I:  |                |                     |                   |                 |                   |                   |                 |  |                   |
| Cu        | $\gamma$ spec. | < 20                | < 20              | -               | < 1.6             | < 1.3             | -               | < 500  | < 200             |
| Si        | NAA            | < $10^{-3}$         | < $10^{-4}$       | -               | -                 | -                 | -               | -  | -                 |
| PTFE      | $\gamma$ spec. | 25(9)               | 30(14)            | 600             | 0.18(6)           | 0.21(10)          | 4.2             | 63(23)   | 45(21)            |
| Phase II: |                |                     |                   |                 |                   |                   |                 |  |                   |
| Cu        | $\gamma$ spec. | < 20                | < 20              | -               | < 0.26            | < 0.26            | -               | < 10   | < 10              |
| Si        | NAA            | < $10^{-3}$         | < $10^{-4}$       | -               | -                 | -                 | -               | -  | -                 |
| PTFE      | $\gamma$ spec. | 50(20)              | 67(25)            | -               | 0.05(2)           | 0.07(3)           | 0.6             | 0.9(4)   | 0.7(3)            |
| CuSn6     | ICPMS          | < 300               | < 300             | 600             | < 0.15            | < 0.15            | -               | < 3  | < 1               |

**Table 9** Activity of the components of the PMT LAr veto system and their estimated background contribution BI at  $Q_{\beta\beta}$  after anti-coincidences but before the LAr veto and PSD.

| Component                    | $^{228}\text{Th}$ | $^{226}\text{Ra}$  | $^{40}\text{K}$     | $\text{BI}(^{208}\text{Tl})$                                   | $\text{BI}(^{214}\text{Bi})$ |
|------------------------------|-------------------|--------------------|---------------------|--|------------------------------|
|                              | $(\mu\text{Bq})$  |                    |                     | $(10^{-6}\text{cts}/(\text{keV}\cdot\text{kg}\cdot\text{yr}))$ |                              |
| PMTs                         | <1940/pc          | <1700/pc           | <9100/pc            | <245   | <33                          |
| voltage dividers             | <500/pc           | <1140/pc           | <11500/pc           | <63  | <22                          |
| SAMI RG178 cables            | <14.4/m           | <11.2/m            | 81(16)/m            |  |                              |
| - along Cu shrouds           |                   |                    |                     | <16  | <2                           |
| - along Fiber shroud         |                   |                    |                     | <227   | <37                          |
| copper shrouds               | 37/kg             | 148/kg             | -                   | 8.6(1)   | 5.7(1)                       |
| Tetratex <sup>®</sup> coated | 70/m <sup>2</sup> | 150/m <sup>2</sup> | 9800/m <sup>2</sup> | 18.2(2)  | 6.4(1)                       |

**Table 10** Activity of the components of the fiber-SiPM LAr veto system and their estimated background contribution BI at  $Q_{\beta\beta}$  after anti-coincidences but before the LAr veto and PSD.

| Component           | method         | $^{228}\text{Th}$ | $^{226}\text{Ra}$ | $^{40}\text{K}$ | mass | $\text{BI}(^{208}\text{Tl})$ | $\text{BI}(^{214}\text{Bi})$                                   |
|---------------------|----------------|-------------------|-------------------|-----------------|------|------------------------------|--|
|                     |                | $(\text{mBq/kg})$ |                   |                 |      | $(\text{g})$                 | $(10^{-6}\text{cts}/(\text{keV}\cdot\text{kg}\cdot\text{yr}))$ |
| fiber BCF-91A       | ICPMS          | 0.058             | 0.042             | 0.46            | 765  | 238                          | 175 (1)  |
| plastic opt.coupl.  | $\gamma$ spec. | 0.15(8)           | < 0.19            | 3.0             | 32   | 7(3)                         | <0.64  |
| SiPM                | ICPMS          | <1                | <3                | -               | 1.3  | <1.8                         | <0.41  |
| Cuflon <sup>®</sup> | $\gamma$ spec. | 0.8(5)            | 1.3(4)            | 18              | 15   | 16(10)                       | 2.1(6)   |
| pins                | $\gamma$ spec. | <5.8              | 15(3)             | 220             | 9.4  | < 74                         | 15(3)  |
| screws              | $\gamma$ spec. | <5.8              | 15(4)             | <120            | 12.7 | <100                         | 20(5)  |
| glue EP601          | $\gamma$ spec. | <1.5              | <0.55             | <13             | 4.0  | <8.1                         | <0.23  |

the components as well as the estimated background contributions of the PMT and fiber systems are given in Tables 9 and 10, respectively.

The specification was that both systems contribute about equally to the BI. The sixteen 3" PMTs and voltage dividers exhibit the largest specific activities although the radiopurity of the PMTs had been further improved in collaboration with the manufacturer, and the potted voltage dividers have been fabricated from selected materials, 0.5 mm Cuflon<sup>®</sup> as printed circuit board and film capacitors rather than ceramic ones. Nevertheless, the PMTs with their voltage dividers had to be mounted at a minimum distance of more than 1 m

from the closest Ge detector in order to stay within the background budget. On the other hand, the very low specific activity of the fibers allows to deploy them, almost 1 kg of material, rather close to the detector array. Altogether, both subdetectors contribute about  $1.2\cdot 10^{-3}\text{cts}/(\text{keV}\cdot\text{kg}\cdot\text{yr})$  to the BI at  $Q_{\beta\beta}$  before LAr veto and PSD; that is more than the Phase II goal. As shown in Section 6 the LAr veto alone suppresses, however, the backgrounds at  $Q_{\beta\beta}$  from  $^{228}\text{Th}$  and  $^{226}\text{Ra}$  sources by factors of about 100 and 6, respectively, resulting in BI values that are fully acceptable for Phase II. Preliminary MC simulations with photon tracking predict indeed an even larger suppression yielding a total

contribution of the LAr veto hardware to the BI at  $Q_{\beta\beta}$  of about  $10^{-5}$  cts/(keV·kg·yr) after LAr veto and PSD cuts.

## 6 Performance

Phase II physics data taking started on December 25, 2015. A first data release PIIa has been presented after about 6 months of running at the Neutrino Conference 2016, and the results have been published in Nature [11]. The following discussion considers the Phase II data taking period up to April 15, 2017. About 6.7% of the total of 477 calendar days were devoted to calibration or maintenance, the rest to physics data taking. A series of nearby earthquakes with magnitudes up to 5.5 slightly affected the ongoing measurements. The exposure taken on tape with the enriched detectors amounts to 43.4 kg·yr which corresponds to a duty factor of more than 93%. Data validation reduces this exposure by 9% to 34.4 kg·yr. As of April 15 2017, all deployed detectors (see Appendix Fig. 33) are operational except the enriched detector GD91C which has a damaged JFET.

The performance of the detector system is characterized in particular by the stability of its energy calibration as well as by the resolutions of the various detector components. It is assessed by regular calibrations and by monitoring continuously the flow of physics data and test pulser events. The following sections present representative examples for the various components and an evaluation of the full system performance including the achieved level of background suppression.

### 6.1 Ge detectors

The operation of bare Ge crystals in LAr is a non-standard technique, and the stability of leakage currents was a major issue in the preparations for Phase I [3]. It was found that passivated detectors - those with a passivation layer in the insulating groove between p<sup>+</sup> contact and the conductive lithium n<sup>+</sup> layer - showed constantly increasing leakage current from repeated calibrations, presumably due to the build up of charges in the groove. Non-passivated detectors did not show this effect, and hence all semi-coaxial detectors deployed in Phase I had the passivation layer removed. To speed up the refurbishment and delivery of the Phase II detectors, the removal of the standard passivation was given up for quite a number of detectors (see yellow colored detectors in Appendix Fig. 33).

Fig. 20 and Fig. 34 of the Appendix show the evolution of the leakage current for all Phase II Ge detectors in the time span between December 2015 and April

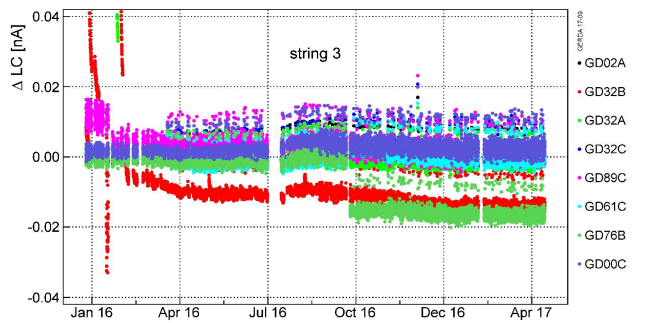


**Fig. 20** Leakage currents of indicated detectors of string 3 in the period from December 2015 to April 2017. For the other detector strings the corresponding data are shown in Fig. 34 of the Appendix.

2017. In the first months, a temporary increase of leakage currents during calibration has been observed for several detectors, passivated and non-passivated ones. This is visible by current spikes reaching up to 300 pA immediately after irradiation; they return to the previous current values within half a day. Except for one detector, the leakage currents of all detectors, both passivated and non-passivated ones, are stable since May 2016 or even reduced compared to the beginning. Hence the number of stable detectors included in the analysis has increased in time. Thus, our experience is strikingly contrary to a former report about ‘the limited long-term stability of naked detectors in LN as result of increasing leakage current’ [33].

#### 6.1.1 Energy scale stability and resolution

Energy calibrations with a  $^{228}\text{Th}$  source are performed regularly, typically once per week; a calibration spectrum is shown in subsection 6.2 (Fig. 27). The energy reconstruction is performed in the off-line analysis of the digitized charge pulses using either a standard semi-Gaussian shaping or, for improved energy resolution, a finite-length zero-area cusp filter [35]. The position of the various peaks are used to establish the energy scale (gain) as well as the resolution as a function of energy. The  $^{208}\text{Tl}$   $\gamma$  line at 2614.5 keV provides a convenient measure to monitor the resolution close to the  $Q_{\beta\beta}$  energy. The upper part of Fig. 21 shows for all detectors the measured FWHM resolutions for this line as well as for its double escape peak (DEP) at 1592.5 keV. The coaxial detectors are in strings 2, 5, and 7. Most of them have a resolution of less than 4.0 keV FWHM. In the period from December 2015 to April 2017 the interpolated average energy resolution at  $Q_{\beta\beta}$  is 3.90(7) keV FWHM, i.e. better than in Phase I (4.8(2) keV). The resolutions of the BEGe detectors show unexpectedly strong variations between 2.5 and 5.6 keV. At  $Q_{\beta\beta}$  the

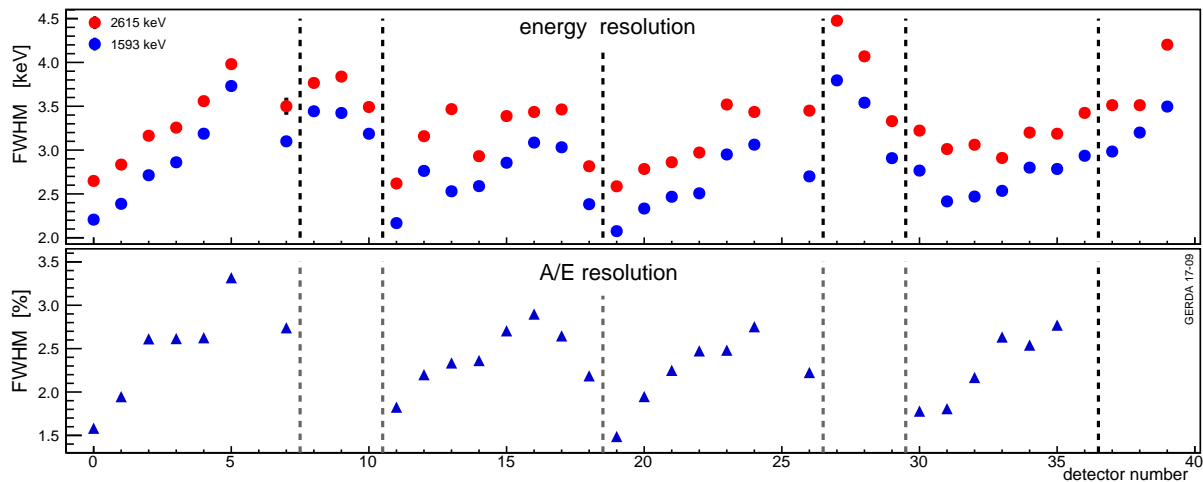


**Fig. 21** FWHM energy resolutions (top) of the 2615 keV line and its DEP at 1593 keV, and A/E resolutions (bottom) of individual Ge detectors deduced from the DEP [34]. The dashed lines separate the 7 detector strings; within each string the detector number increases from top to bottom detector.

interpolated mean is 2.93(6) keV which is also better than in Phase I (3.2(2) keV). The top detector in each string exhibits indeed the expected resolution well below 3 keV but there is a consistent trend of decreasing resolution when going down in the string. This effect has not been observed in Phase I where single wires were used for the signal readout instead of the FFCs in Phase II. Thus larger stray capacitances with increasing cable length and capacitive coupling within the readout cable bundle of a string might explain the observation. A good understanding of the resolution pattern is, however, still lacking and further work on this issue is in progress.

The stability of the energy scale is not only verified by calibration measurements but continuously monitored by injecting every 20 s a test charge into the electronic front ends. If the gain variation is larger than 0.1%, an extra unscheduled calibration with the  $^{228}\text{Th}$  source is taken. Fig. 22 shows for the period from December 2015 to April 2017 the shifts of the 2615 keV calibration peak between successive calibrations. Most data points are within the range of  $\pm 1\sigma \approx \pm 1.5$  keV; this is sufficient to allow the merging of the data from all periods (periods with shifts exceeding 2 keV are discarded from analysis).

### 6.1.2 Pulse shape discrimination efficiencies

The new Ge detectors for Phase II have been chosen to be of the BEGe type because the time profile of its current pulse allows for a powerful but simple discrimination between  $0\nu\beta\beta$ -like events, i.e. localized single-site events (SSEs), from background events which have often multiple energy depositions (multi-site events, MSEs)

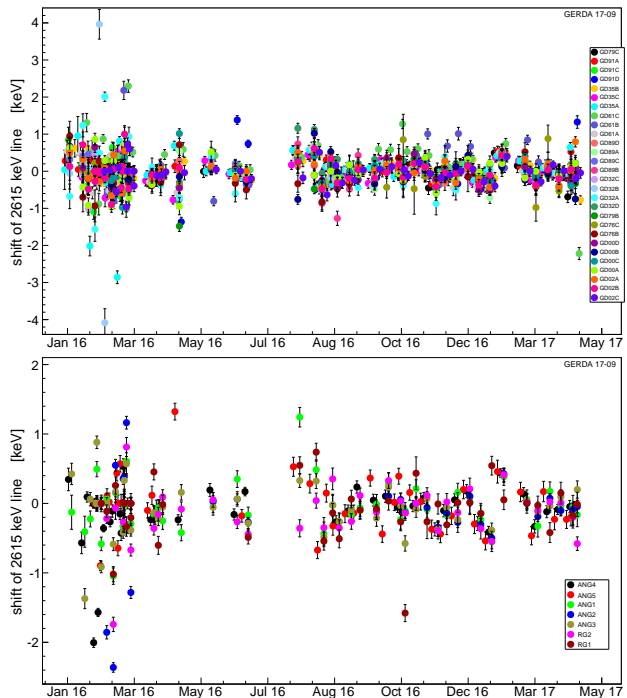


**Fig. 22** Shift of the 2615 keV peak of  $^{208}\text{Tl}$  between consecutive calibrations for indicated BEGe (top) and enriched coaxial detectors (bottom).

or occur at the detector surface [12]. It is based on a single parameter, the ratio A/E of the maximum of the current pulse A over the total energy E. SSEs are identified by an (normalized) A/E value of about 1, MSEs and events on the  $n^+$  surface by a value lower than 1, and surface events at the  $p^+$  contact like  $\alpha$  particles by  $A/E > 1$ . Like in Phase I the A/E cut is calibrated with the data from the weekly calibrations with the

$^{228}\text{Th}$  source. Events in the DEP are used as a proxy for  $0\nu\beta\beta$  events. The inset in  $^{228}\text{Th}$  calibration spectrum (Fig. 27) illustrates the effect of the  $A/E\sim 1$  cut (yellow colored spectrum): the obvious survival of the DEP at 1593 keV and the distinct suppression of the single gamma line of  $^{212}\text{Bi}$  at 1621 keV.

While a detailed account of the PSD analysis of Phase II data is in preparation we discuss here just some differences compared to the analysis of the Phase I data. To select signal-like events a two-sided  $A/E$  cut is applied: MSE and  $n^+$  surface events are removed by a cut on the low  $A/E$  side, while events on the  $p^+$  contact are rejected by a high  $A/E$  cut. The lower part of Fig. 21 shows the strong variation of the  $A/E$  resolution of individual BEGe detectors following a similar trend as the energy resolution. The  $A/E$  resolutions differ for individual detectors by up to a factor of 2, and they are often significantly worse than in Phase I where they varied between 1.5 % and 1.9 %. Moreover, to reach the Phase II BI goal of  $10^{-3}$  cts/(keV·kg·yr), a stronger low  $A/E$  cut for higher suppression of MSE compared to Phase I is applied. Hence, other than in Phase I, individual cuts have been applied to each detector accounting for the increased noise.

The low  $A/E$  cut is chosen according to 90 % acceptance of the DEP events. Fig. 23 shows for each BEGe detector and its respective  $A/E$  cuts the survival fractions for various energy and peak regions in the  $^{228}\text{Th}$  spectrum. The survival fractions in the peak and Compton regions increase from top to bottom in the respective detector strings, reflecting the deterioration of the  $A/E$  resolution from top to bottom. For further suppression of surface events, a high  $A/E$  cut with twice the separation from  $A/E = 1$  as the lower cut is applied.

Table 11 provides a summary from the combined data of all BEGe detectors and calibration runs. The survival fraction of Compton events from  $^{208}\text{Tl}$  is 45.3 % at  $Q_{\beta\beta}$ . Full energy  $\gamma$  peaks (FEPs) are suppressed to less than 15 %. The strongest suppression (11 %) is achieved for single escape peaks (SEPs) which exhibit a relatively large MSE component. The high  $A/E$  cut reduces the survival fractions of events in the DEP and  $Q_{\beta\beta}$  region by less than 5 %.

## 6.2 LAr veto

In ultra-pure LAr the scintillation light yield is about  $41\cdot 10^3$  photons per 1 MeV electron-equivalent energy deposition for the fast and slow (triplet) component of the Ar excimer [36]. The purity of LAr has a strong influence on the light yield affecting predominantly the light emitted from the triplet state whose lifetime can thus be taken as a good indication for the LAr purity.

**Table 11** Rejected event fractions by the low and high  $A/E$  cuts, and the survival fractions (s.f.) from all BEGe detectors and calibration runs [34].

| region              | low cut (%) | high cut (%) | s.f. (%) |
|---------------------|-------------|--------------|----------|
| DEP(1593)           | 10.0(2)     | 2.68(6)      | 87.3(2)  |
| FEP(1621)           | 83.5(3)     | 1.62(8)      | 14.9(3)  |
| FEP(2615)           | 83.58(3)    | 1.82(1)      | 14.60(2) |
| SEP(2104)           | 87.8(2)     | 1.55(4)      | 10.6(2)  |
| (2039 $\pm$ 35) keV | 52.5(1)     | 2.20(2)      | 45.3(1)  |

For ultra-pure LAr, it is 1590(100) ns [37]. The triplet lifetime of the LAr contained in the GERDA cryostat has been deduced by averaging the waveforms (see Fig. 18) acquired with the PMTs of the LAr veto system and fitting the slow exponential tail (Fig. 24). The fit yields a value of 968(11) ns, indicating a still acceptable LAr purity after almost 6 years of operation without a significant refill and any purification.

The LAr veto system is running stably with all PMT and SiPM channels fully functional since March 2016. Before this date, 2 PMTs were not operational due to contact problems outside the lock system. During commissioning the LAr veto system has been immersed into the cryostat (and warmed up) more than 20 times. No ageing effects have been observed since its first deployment in April 2015.

The dark rate in the individual PMTs and SiPM channels is 300-500 Hz and  $<200$  Hz, respectively. It is mostly due to the  $\beta$  decay ( $Q_{\beta}=565$  keV) of  $^{39}\text{Ar}$  ( $8\cdot 10^{-16}$  abundance relative to the stable  $^{40}\text{Ar}$ ) with an activity of  $\sim 1$  Bq/kg of  $^{40}\text{Ar}$  [38]. The resulting dead time is about 2 %. Note that the radon shroud [3] limits the field of view of the SiPM-fiber assembly in the cryostat to radii of less than 37.5 cm; our preliminary estimate for the attenuation length is  $\sim 15$  cm.

The stability and noise level of the LAr veto system is continuously monitored with physics data. Figs. 25 and 26 show on top a typical pulse height spectrum for a PMT and SiPM channel, respectively; and at bottom the scatter plots from which these pulse height spectra have been deduced. These data have been accumulated in coincidence with Ge triggers during a time span of about 16 months. The noise levels and gains are obviously stable, and the clear separation between noise and single photoelectron (PE) peak leads to a straightforward setting of the veto thresholds, indicated by the red lines, that can be easily readjusted if the gain jumps. These settings are 0.2-0.35 PE for PMTs, and 0.4-0.6 PE for SiPMs; the threshold is higher for only one PMT channel (0.6 PE) and one SiPM channel (0.9 PE) where the individual SiPMs exhibit slightly different gains.

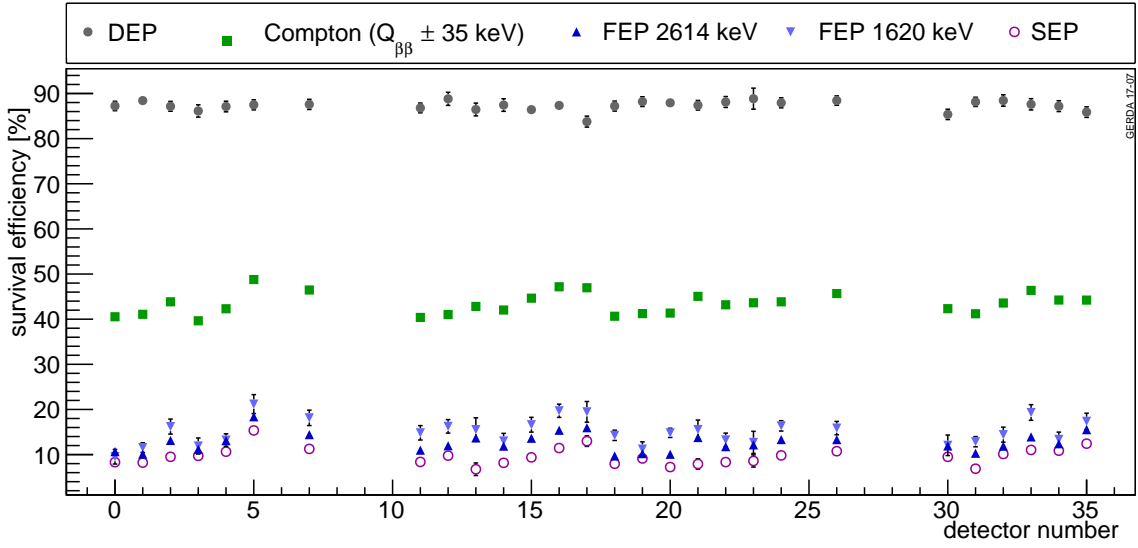


**Fig. 23** Survival efficiencies for the double escape (DEP) and single escape peak (SEP) of the 2615 keV  $\gamma$  line of  $^{208}\text{Tl}$ , for the full energy  $\gamma$  peaks (FEPs) at 1620 keV and 2615 keV, and the Compton events around  $Q_{\beta\beta}$  [34]. Uncertainties are partly smaller than the symbols.

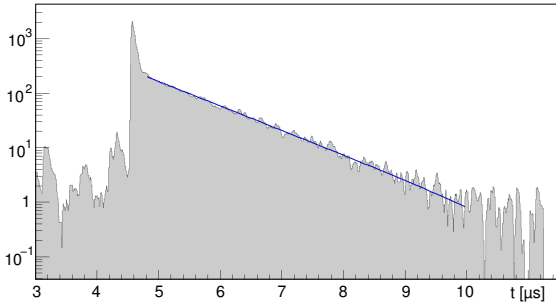


**Fig. 24** Average PMT waveform recorded on 30.09.2015 in the LAr of the GERDA cryostat. The solid line indicates the triplet lifetime fit with a decay time of 0.97  $\mu\text{s}$  [24].

The performance of the LAr veto system has been tested with both a  $^{228}\text{Th}$  and  $^{226}\text{Ra}$  source. Fig. 27 shows the measured spectra as obtained after standard quality cuts, and after indicated additional cuts. Both spectra exhibit the same specific features that have been observed in the LARGE test stand; for a detailed discussion see [21]. One highlight is displayed in the inset of the  $^{228}\text{Th}$  spectrum (Fig. 27, l.h.s.). The DEP of the  $^{208}\text{Tl}$  2615 keV  $\gamma$  line at 1593 keV is barely suppressed by PSD ( $\approx 90\%$  acceptance) while the LAr veto cut eliminates it completely due to the two escaping 511 keV annihilation quanta. On the other hand, the  $^{212}\text{Bi}$  single  $\gamma$  line at 1621 keV is largely accepted by the LAr veto because the full energy is deposited in the Ge detector.

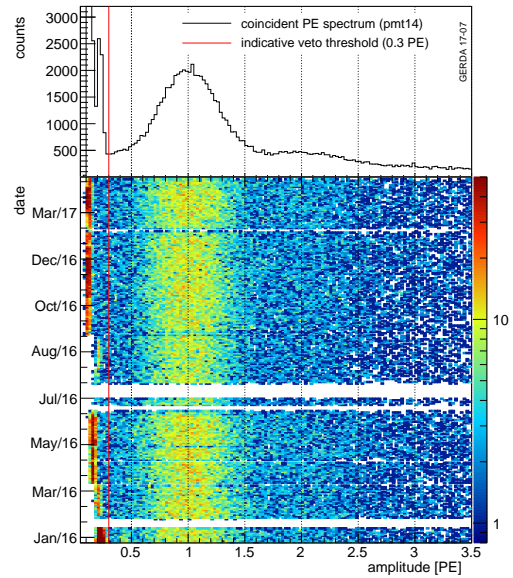


**Fig. 25** Pulse height spectrum of a PMT (top) deduced from the scatter plot (bottom) which has been accumulated between January 2016 and April 2017.

The  $^{208}\text{Tl}$  2615 keV  $\gamma$  line as well as the various  $^{214}\text{Bi}$   $\gamma$  lines in the  $^{226}\text{Ra}$  spectrum (Fig. 27, r.h.s.) provide significant contributions to the background around  $Q_{\beta\beta}$  [10], and hence the suppression of the continuum around  $Q_{\beta\beta}$  is of special interest. The respective suppression factors are collected in Table 12. While the suppression by PSD is comparable, a much stronger suppression by the LAr veto for  $^{228}\text{Th}$  than for  $^{226}\text{Ra}$  is noticed. This can be understood since for  $^{226}\text{Ra}$  the

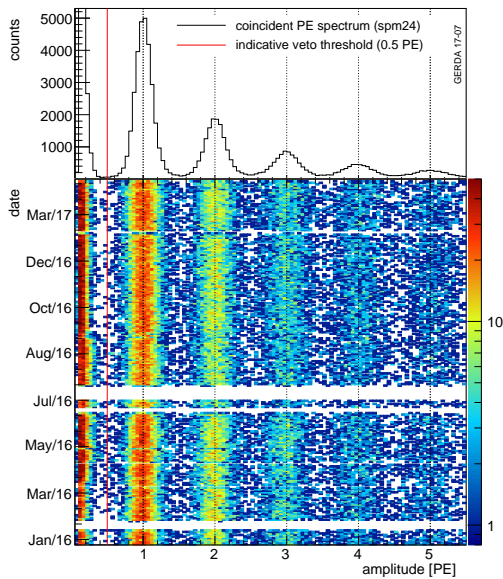


**Fig. 26** Same as Fig. 25 but for a SiPM channel representing 6 SiPMs read out in parallel.

**Table 12** Suppression factors obtained in the ROI with a  $^{228}\text{Th}$  and  $^{226}\text{Ra}$  source from Ge anti-coincidences (anti), the LAr veto (LAr), pulse shape discrimination (PSD), and after all cuts (all); the acceptance (acc.) values refer to all cuts.

| Source            | anti    | LAr    | PSD     | all     | acc.  |
|-------------------|---------|--------|---------|---------|-------|
| $^{228}\text{Th}$ | 1.26(1) | 98(4)  | 2.19(1) | 345(25) | 0.868 |
| $^{226}\text{Ra}$ | 1.26(1) | 5.7(2) | 2.98(6) | 29(3)   | 0.899 |

main contribution to the Compton continuum is due to the 2204 keV single  $\gamma$  line so that less than 200 keV are available for deposition in the LAr; in case of  $^{228}\text{Th}$ , however, the more energetic 2615 keV  $\gamma$  ray is accompanied in 86 % of the cases by a 583 keV  $\gamma$  ray so that more energy is available for deposition in the LAr. In general, our measured suppression factors are smaller than the ones obtained in LArGE [21]. This might be due to several reasons, e.g. different geometry with different shadowing conditions, different radioactive sources with different leakage of  $\beta$  particles, and, definitely, lower purity of the LAr.

The performance of the LAr veto system can be monitored continuously with the two strongest  $\gamma$  lines of the physics data (Fig. 28, see also Fig. 30). The  $\gamma$  line at 1525 keV is due to the decay of  $^{42}\text{K}$ , a  $\beta$ - $\gamma$  cascade, in which the  $\beta$  particle can deposit up to 2 MeV in the LAr. The LAr veto system suppresses this line by typically a factor of 5. On the other hand, the  $^{40}\text{K}$  line at 1461 keV, a single  $\gamma$  line, is not suppressed since it follows electron capture of  $^{40}\text{K}$  without any energy deposition in the LAr. Hence, no suppression is expected

apart from random coincidences so that this line can be used to determine the LAr veto acceptance independently of the pulser.

### 6.3 Muon veto system

Fig. 29 shows for 16 months in 2016/17 the daily rate of one PMT of each of the seven PMT rings in the water tank [3], i.e. of varying height in the water. Only the standard trigger requirements are requested: either 5 Cherenkov PMTs within 60 ns with a signal above threshold of 0.5 PE, or a triple coincidence within the plastic veto. A mean stability of 4 % can be observed. No readjustment of the HV was necessary during the 477 days of operation of Phase II. The mean daily rate of 3164(6) muons was measured which translates into a rate of  $3.54 \cdot 10^{-4}/(\text{m}^2 \cdot \text{s})$ . This is a 1.8 % deviation from the mean of Phase I [39], still consistent and giving hints on systematic uncertainties.

A further proof of the reliability of the muon veto performance comes through the analysis of the muon seasonal variation. Despite the shorter measurement period essentially the same parameters were derived as previously [39].

### 6.4 Background levels

#### 6.4.1 Spectra

Fig. 30 shows the exposure-normalized Phase II background spectra obtained with the BEGe and enriched semi-coaxial detectors after quality cuts but before LAr veto and PSD. Both spectra agree well, exhibiting the same prominent features as observed in Phase I: below 500 keV the tail of the  $^{39}\text{Ar}$   $\beta$ -spectrum, between 600 keV and 1600 keV the broad structure from the  $2\nu\beta\beta$  decays, individual  $\gamma$ -lines between 400 and 2650 keV, and  $\alpha$ -structures above 3500 keV predominantly due to  $^{210}\text{Po}$  and  $^{226}\text{Ra}$  decays.

The observed differences for the tail of the  $^{39}\text{Ar}$   $\beta$ -spectrum originate from the different dead layers in BEGe and coaxial detectors, in particular from the large and thin  $\text{p}^+$  contact in the bore hole of the latter detector type.

The pulse shapes of the observed  $\alpha$ -events reveal them to be predominantly located at the surface of the  $\text{p}^+$  contact. While the count rate is relatively low and similar in case of the BEGe detectors, it is larger for the coaxial ones where one detector (ANG4) contributes more than 50% to the total rate. The origin of the contamination is not understood, but there is evidence that it occurred during the fabrication process.

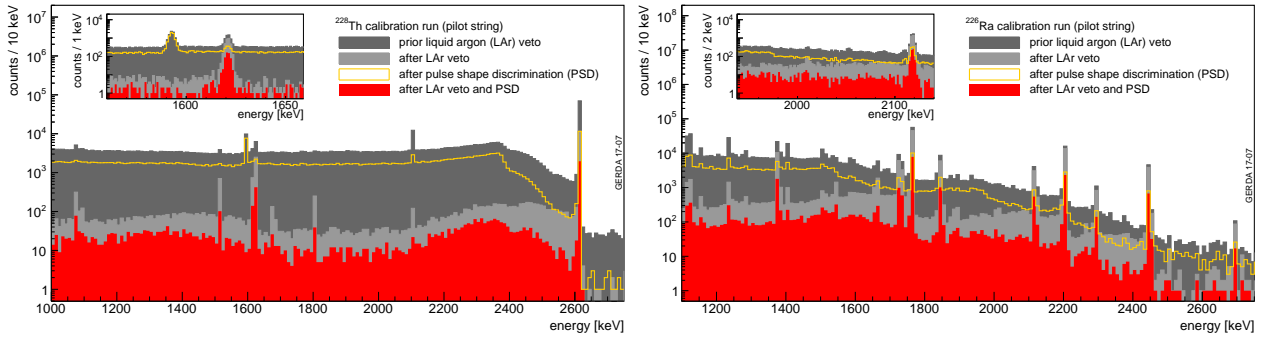


**Fig. 27** Calibration spectra for  $^{228}\text{Th}$  (left) and  $^{226}\text{Ra}$  (right) with detector anti-coincidence and muon veto (dark grey), with suppression by the LAr veto system and pulse shape discrimination (PSD), and by the combination of LAr veto system and PSD. The inset on the l.h.s. shows the double escape peak of  $^{208}\text{Tl}$  at 1593 keV and the 1621 keV single gamma line of  $^{212}\text{Bi}$ , on the r.h.s. the 2118 keV single gamma line of  $^{214}\text{Bi}$ .

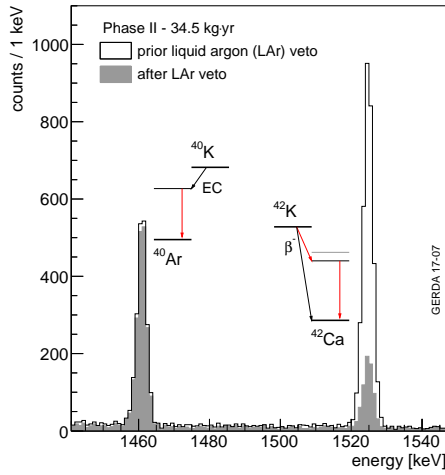


**Fig. 28** Monitoring the LAr veto performance with the  $^{40}\text{K}$  and  $^{42}\text{K}$   $\gamma$  lines (see text).

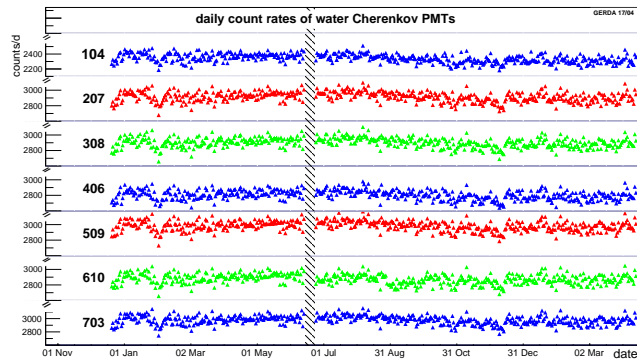


**Fig. 29** Daily rates of water Cherenkov PMTs, one from each ring (c.f. Ref. [40]).

#### 6.4.2 Intensity of $\gamma$ lines

The intensities of the  $\gamma$  lines carry information about the nature and location of various contamination sources [10]. While the detailed model study of the background is in

progress, we note here that the count rates of the  $^{40}\text{K}$  and  $^{42}\text{K}$  lines are increased strongly in Phase II, by factors of 4 and 2 compared to Phase I, respectively. Since the lines are located well below  $Q_{\beta\beta}$  they will not affect the background index. The increased  $^{40}\text{K}$  intensity might be due to the different kind and increased number of cables which run in Phase II along the detector array as well as to the LAr veto system. The increased  $^{42}\text{K}$  intensity is understood qualitatively by the change from metallic to plastic mini-shrouds. The latter no longer shield the electric fields of the Ge detectors so that more  $^{42}\text{K}$  ions can be attracted closer to the detectors. For all other  $\gamma$  lines the count rates are similar to those observed in Phase I; the intensities of the  $^{214}\text{Bi}$   $\gamma$ -lines is even lower than in Phase I. This is a remarkable success considering the additional amount of material that has been deployed in Phase II close to the detector array.

#### 6.4.3 Background index at $Q_{\beta\beta}$

Table 13 collects data in the analysis window<sup>8</sup> around  $Q_{\beta\beta}$  which are used to extract the BI in Phase II. In addition, to the Phase IIa data (December 2015 - June 2016) of the first data release [11], data of subsequent physics runs until April 2017 (Phase IIb) are shown which exhibit a more than 50% larger exposure. These data with higher statistics confirm the BI reported from the first data release with increased significance yielding in total  $(2.7^{+1.1}_{-0.8}) \cdot 10^{-3}$  cts/(keV·kg·yr) for the coaxial and  $(1.0^{+0.6}_{-0.4}) \cdot 10^{-3}$  cts/(keV·kg·yr) for the BEGe detectors. This corroborates that the goal of the Phase II

<sup>8</sup>The analysis window extends from 1930 keV to 2190 keV excluding the intervals 2104(5) keV and 2119(5) keV of known  $\gamma$  lines from  $^{208}\text{Tl}$  (SEP) and  $^{214}\text{Bi}$ . In addition, the 50 keV wide blinded interval centered at  $Q_{\beta\beta}$  is excluded for the Phase IIb coaxial data which are not yet unblinded.



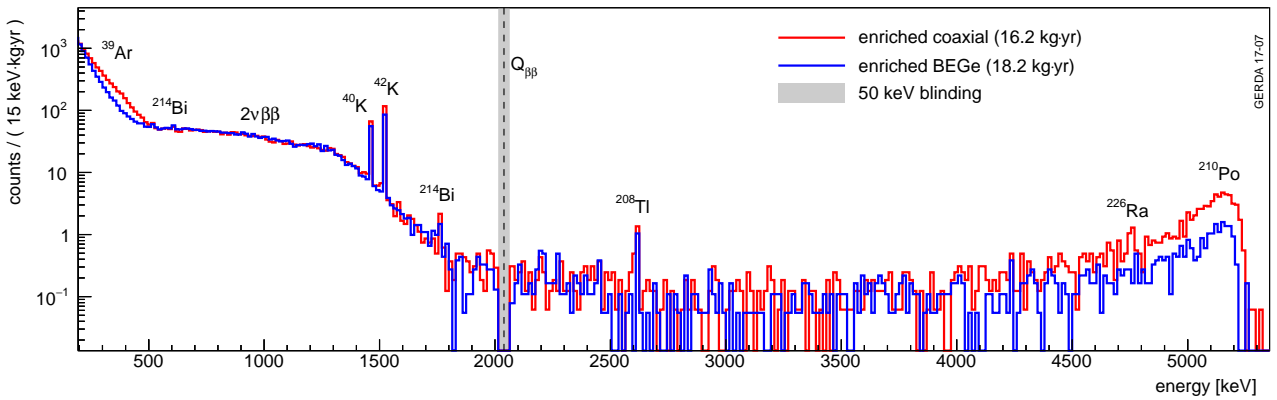


**Fig. 30** Normalized GERDA Phase II background spectra from BEGe and enriched coaxial detectors before pulse shape discrimination and LAr veto. The grey bar indicates the blinded energy region around  $Q_{\beta\beta}$ .

**Table 13** Counts in the analysis window observed in Phase IIa and IIb with indicated exposures  $\mathcal{E}$  after anti-coincidences within the detector array (AC), after anti-coincidences and LAr veto (LAr) or pulse shape discrimination (PSD), and after all cuts (all). The quoted background indices BI in units (biu) of  $10^{-3}$  cts/(keV·kg·yr) have been determined after all cuts; the uncertainties are statistical and deduced for a Poissonian signal.

| det/phase | $\mathcal{E}$<br>(kg·yr) | AC<br>cts | LAr<br>cts | PSD<br>cts | all<br>cts | BI<br>(biu)         |
|-----------|--------------------------|-----------|------------|------------|------------|---------------------|
| Coax/IIa  | 5.0                      | 19        | 12         | 8          | 4          | $3.5^{+2.1}_{-1.5}$ |
| /IIb*     | 11.2                     | 38        | 14         | 17         | 5          |                     |
| total*    | 16.2                     | 57        | 26         | 25         | 9          | $2.7^{+1.0}_{-0.8}$ |
| BEGe/IIa  | 5.8                      | 21        | 6          | 5          | 1          | $0.7^{+1.1}_{-0.5}$ |
| /IIb      | 12.4                     | 30        | 11         | 6          | 3          |                     |
| total     | 18.2                     | 51        | 17         | 11         | 4          | $1.0^{+0.6}_{-0.4}$ |

\* Values preliminary since PSD cuts are not yet finalized.

upgrade, an improvement of the BI by a factor of 10 compared to Phase I, has been achieved.

Table 13 shows also the counts in the analysis window after various cuts. After anti-coincidences within the detector array these counts correspond to a BI below  $(1-2) \cdot 10^{-2}$  cts/(keV·kg·yr) for both BEGe and coaxial detectors. Within the limited statistics, the LAr veto and PSD seem to suppress background events with comparable strength. As first evidence for various contributing suppression mechanisms it is noted that of the 108 events surviving the anti-coincidence cut, 23 resp. 30 events are cut exclusively by the LAr veto and PSD, while 42 events are cut by both LAr veto and PSD.

## 7 Conclusion

GERDA continues to exploit novel technologies in order to study neutrinoless double beta decay of  $^{76}\text{Ge}$  with unprecedented low background rate. Operating in

Phase I for the first time about 18 kg of bare enriched Ge detectors in LAr, it achieved a background index of  $10^{-2}$  cts/(keV·kg·yr), reaching a sensitivity of  $2.4 \cdot 10^{25}$  yr after an exposure of 21.6 kg·yr, and setting the most stringent  $0\nu\beta\beta$  half-life limit for  $^{76}\text{Ge}$ .

In order to reach the goal of Phase II, a further reduction of the background index by another order of magnitude to  $10^{-3}$  cts/(keV·kg·yr), two major pioneering measures have been taken: (i) the instrumentation of the LAr surrounding the detectors with PMTs and fibers read out by SiPMs; this allows the identification and vetoing of background events by the scintillation light from their energy deposition in the LAr, and (ii) the deployment of an additional 20 kg of enriched BEGe detectors that exhibit superior pulse shape discrimination and energy resolution compared to the coaxial detector type prevailing in Phase I. These actions necessitated an upgrade of several infrastructure components respecting thereby the strict requirements on the radiopurity of the newly introduced materials. Affected components include lock, cabling, detector mounts and replacement of the copper mini-shrouds by transparent ones.

The upgrade to Phase II including commissioning was concluded at the end of 2015 and the experiment is taking physics data with a duty factor of more than 90% since. Both the Ge detectors as well as the LAr veto system exhibit stable operation within specifications. The leakage currents of 39 out of the 40 deployed Ge detectors are stable since more than one year of continuous operation in LAr, and often even reduced compared to the beginning. At  $Q_{\beta\beta}$  the interpolated energy resolution of coaxial and BEGe detectors is on average 3.90(7) keV and 2.93(6) keV FWHM, respectively. Regular calibrations establish the gain drifts of the Ge detector readout chains to be smaller than 1.5 keV around  $Q_{\beta\beta}$ , i.e. to stay within  $\pm 1\sigma$  of the energy resolution;

this allows to combine data sets accumulated during more than one year without significant deterioration of energy resolution. The combined data from these calibrations runs are used to optimize event selection criteria and efficiencies of pulse shape discrimination. The performance of the LAr veto system has been established by dedicated calibrations runs with  $^{228}\text{Th}$  and  $^{226}\text{Ra}$  sources yielding suppression factors at  $Q_{\beta\beta}$  of about 100 and 6, respectively. Quasi-continuous monitoring during the physics runs is achieved by analysis of the relatively strong  $^{40}\text{K}$  and  $^{42}\text{K}$   $\gamma$  lines at 1461 keV and 1525 keV.

Based on an exposure of 10.8 kg $\cdot$ yr results of a first period of the Phase II physics run have been published recently [11]. They demonstrate that the goal of Phase II, a background index of about  $10^{-3}$  cts/(keV $\cdot$ kg $\cdot$ yr), has been achieved. This finding is statistically corroborated here with data from a more than doubled exposure of 23.6 kg $\cdot$ yr. GERDA will thus remain background-free up to its design exposure of 100 kg $\cdot$ yr reaching thereby a sensitivity beyond  $10^{26}$  yr.

## References

1. R.N. Mohapatra et al., Rept. Prog. Phys. 70 (2007) 1757
2. C. Patrignani et al. (Particle Data Group), Chin. Phys. C, 40, (2016):100001, p. 767
3. K.-H. Ackermann et al. [GERDA collaboration] Eur. Phys. J. C 73 (2013) 2330
4. M. Giammarchi et al., AIP Conference Proceedings 1549 (2013) 209
5. A. Caldwell and K. Kroeninger, Phys. Rev. D 74 (2006) 092003
6. M. Agostini et al. [GERDA collaboration] Phys. Rev. Lett. 111 (2013) 122503
7. H.V. Klapdor-Kleingrothaus, I.V. Krivovheina, A. Dietz, and O. Chkvorets, Phys. Lett. B586 (2004) 198 - 212; H.V. Klapdor-Kleingrothaus and I.V. Krivovheina, Mod. Phys. Lett. A21 (2006) 1547 - 1566
8. M. Agostini et al. [GERDA collaboration] Eur. Phys. J. C 75 (2015) 416
9. M. Agostini et al. [GERDA collaboration], J. Phys. G: Nucl. Part. Phys. 42 (2015) 115201
10. M. Agostini et al. [GERDA collaboration] Eur. Phys. J. C 74 (2014) 2764
11. M. Agostini et al. [GERDA collaboration] Nature 544 (2017) 47
12. M. Agostini et al. [GERDA collaboration] Eur. Phys. J. C 73 (2013) 2583
13. M. Barnabe Heider, Dissertation, Universität Heidelberg (2009), DOI: 10.11588/heidok.00009551
14. M. Agostini et al. [GERDA collaboration] Eur. Phys. J. C 75 (2015) 39
15. E. Andreotti et al., J. Instrum. 8 (2013) P06012
16. T. Bode, Dissertation, Technische Universität München (2016)
17. S. Riboldi, A. Pullia, and C. Cattadori, Nuclear Science Symposium and Medical Imaging Conference (NSS/MIC), 2012 IEEE, pp. 782-785 DOI: 10.1109/NSS-MIC.2012.6551209
18. S. Riboldi et al., 2015 4th International Conference on Advancements in Nuclear Instrumentation Measurement Methods and their Applications (ANIMMA 2015) pp. 1, DOI: 10.1109/ANIMMA.2015.7465549
19. A. Lubashevskiy et al., submitted to Eur. Phys. J. C, preprint: <https://arxiv.org/abs/1708.00226>
20. J. Benziger et al., Nucl. Instrum. Meth. A582 (2007) 509
21. M. Agostini et al., Eur. Phys. J. C 75 (2015) 506
22. J. Janicskó Csáthy et al., Nucl. Instr. Methods 654 (2011) 225, and arxiv:1606.04254
23. L. Baudis, G. Benato, R. Dressler, F. Piastra, I. Usoltsev and M. Walter, J. Instrum. 10 (2015) P09009
24. A. Wegmann, Dissertation, Universität Heidelberg (2017), DOI: 10.11588/heidok.00022568
25. M. Heisel, Dissertation, Universität Heidelberg (2011), URN: urn:nbn:de:bsz:16-opus-119216
26. M. Agostini, L. Pandola, P. Zavarise and O. Volynets, J. Instrum. 6 (2011) P08013
27. K. Freund et al., Eur. Phys. J. C 76 (2016) 298
28. L. Baudis, A.D. Ferella, F. Froborg, and M. Tarka, Nucl. Instr. Methods A 729 (2013) 557
29. L. Baudis et al., J. Instrum. 10 (2015) P12005
30. T. Goldbrunner, Dissertation, Technische Universität München (1997)
31. M. L. di Vacri et al., AIP Conf. Proc. 1672 (2015) 150001
32. B. Lehnert, Dissertation, Universität Dresden (2016)
33. H.V. Klapdor-Kleingrothaus and I.V. Krivosheina, Nucl. Instrum. Meth. A 566 (2006) 472
34. V. Wagner, Dissertation, Universität Heidelberg (2017), DOI: 10.11588/heidok.00022621
35. M. Agostini et al., [GERDA collaboration], Eur. J. Phys. C 75 (2015) 255
36. T. Doke et al., Nucl. Instrum. Meth. 269 (1988) 291
37. A. Hitachi and T. Takahashi, Phys. Rev. B 27 (1983) 5279
38. P. Benetti et al., Nucl. Instrum. Meth. A574 (2007) 83
39. M. Agostini et al. [GERDA collaboration], Astroparticle Physics 84 (2016) 29
40. Masterarbeit, J. Knies, University Tübingen (2016)
41. R. Brugnera et al., J. Instrum. 7 (2012) P10017

**Acknowledgements** The GERDA experiment is supported by the German Federal Ministry for Education and Research (BMBF), the German Research Foundation (DFG) via the Excellence Cluster Universe, the Italian Istituto Nazionale di Fisica Nucleare (INFN), the Max Planck Society (MPG), the Polish National Science Centre (NCN), the Foundation for Polish Science (TEAM/2016-2/17), the Russian Foundation for Basic Research (RFBR) and the Swiss National Science Foundation (SNF). These research institutions acknowledge internal financial support.

This project has received funding/support from the European Union's Horizon 2020 research and innovation programme under the Marie Skłodowska-Curie grant agreements No 690575 and No 674896.

The GERDA Collaboration thanks the directors and the staff of the LNGS for their support of the GERDA experiment.

## Appendix

**Table 14** Main parameters of all detectors used in GERDA Phase II. The GD, ANG and RG detectors are made of germanium enriched in  $^{76}\text{Ge}$  from 85.5% to 88.3%. The three GTF detectors are made from natural germanium. The operational voltages recommended by the manufacturer are quoted. A ‘y’ marks in column 4 the detectors with a passivation layer (PL) in the groove. The position number in a given string increases from top to bottom. The active masses of the newly produced BEGe detectors include a correction that considers a full charge collection depth growth occurred during storage at room temperature in the three years before deployment in GERDA. Finally, the full energy peak detector efficiencies  $\epsilon_{fep}$  for the  $0\nu\beta\beta$  decay in  $^{76}\text{Ge}$  are quoted.

| Nr. | Detector           | $V_{rec}$<br>[kV] | With<br>PL | String &<br>Position | $f_{Ge76}$        | $M_{diode}$<br>[g] | $M_{av}$ $\begin{smallmatrix} +ucorr+corr \\ -ucorr-corr \end{smallmatrix}$<br>[g] | $\epsilon_{fep} \pm ucorr \pm corr$ |
|-----|--------------------|-------------------|------------|----------------------|-------------------|--------------------|--|-------------------------------------|
| 13  | GD32A              | 3.0               |            | III-2                | $0.877 \pm 0.013$ | 458                | $404 \begin{smallmatrix} +10+4 \\ -10-2 \end{smallmatrix}$                         | $0.888 \pm 0.001 \pm 0.002$         |
| 12  | GD32B              | 4.0               |            | III-1                | $0.877 \pm 0.013$ | 716                | $632 \begin{smallmatrix} +10+4 \\ -10-2 \end{smallmatrix}$                         | $0.900 \pm 0.001 \pm 0.002$         |
| 14  | GD32C              | 4.0               |            | III-3                | $0.877 \pm 0.013$ | 743                | $665 \begin{smallmatrix} +10+4 \\ -10-2 \end{smallmatrix}$                         | $0.901 \pm 0.001 \pm 0.002$         |
| 34  | GD32D              | 4.0               |            | VI-4                 | $0.877 \pm 0.013$ | 720                | $657 \begin{smallmatrix} +10+5 \\ -10-2 \end{smallmatrix}$                         | $0.900 \pm 0.001 \pm 0.002$         |
| 24  | GD35A              | 4.0               |            | IV-5                 | $0.877 \pm 0.013$ | 768                | $693 \begin{smallmatrix} +13+3 \\ -13-2 \end{smallmatrix}$                         | $0.904 \pm 0.001 \pm 0.002$         |
| 1   | GD35B              | 4.0               |            | I-1                  | $0.877 \pm 0.013$ | 810                | $740 \begin{smallmatrix} +11+5 \\ -11-2 \end{smallmatrix}$                         | $0.902 \pm 0.001 \pm 0.002$         |
| 19  | GD35C              | 3.5               | y          | IV-0                 | $0.877 \pm 0.013$ | 634                | $572 \begin{smallmatrix} +9+4 \\ -9-3 \end{smallmatrix}$                           | $0.893 \pm 0.001 \pm 0.002$         |
| 4   | GD61A              | 4.5               | y          | I-4                  | $0.877 \pm 0.013$ | 731                | $652 \begin{smallmatrix} +12+4 \\ -11-3 \end{smallmatrix}$                         | $0.902 \pm 0.001 \pm 0.002$         |
| 26  | GD61B              | 4.0               | y          | IV-7                 | $0.877 \pm 0.013$ | 751                | $666 \begin{smallmatrix} +12+5 \\ -12-2 \end{smallmatrix}$                         | $0.899 \pm 0.001 \pm 0.002$         |
| 16  | GD61C              | 4.0               |            | III-5                | $0.877 \pm 0.013$ | 634                | $562 \begin{smallmatrix} +10+5 \\ -10-3 \end{smallmatrix}$                         | $0.892 \pm 0.001 \pm 0.002$         |
| 17  | GD76B              | 3.5               | y          | III-6                | $0.877 \pm 0.013$ | 384                | $326 \begin{smallmatrix} +7+3 \\ -7-2 \end{smallmatrix}$                           | $0.883 \pm 0.001 \pm 0.002$         |
| 20  | GD76C              | 3.5               | y          | IV-1                 | $0.877 \pm 0.013$ | 824                | $723 \begin{smallmatrix} +12+5 \\ -12-2 \end{smallmatrix}$                         | $0.902 \pm 0.001 \pm 0.002$         |
| 32  | GD79B              | 3.5               |            | VI-2                 | $0.877 \pm 0.013$ | 736                | $648 \begin{smallmatrix} +13+5 \\ -13-2 \end{smallmatrix}$                         | $0.897 \pm 0.001 \pm 0.002$         |
| 23  | GD79C              | 3.5               |            | IV-4                 | $0.877 \pm 0.013$ | 812                | $713 \begin{smallmatrix} +13+5 \\ -11-2 \end{smallmatrix}$                         | $0.900 \pm 0.001 \pm 0.002$         |
| 35  | GD89A              | 4.0               |            | VI-5                 | $0.877 \pm 0.013$ | 524                | $462 \begin{smallmatrix} +10+3 \\ -9-2 \end{smallmatrix}$                          | $0.893 \pm 0.001 \pm 0.002$         |
| 5   | GD89B              | 3.5               | y          | I-5                  | $0.877 \pm 0.013$ | 620                | $533 \begin{smallmatrix} +12+4 \\ -12-2 \end{smallmatrix}$                         | $0.890 \pm 0.001 \pm 0.002$         |
| 15  | GD89C              | 4.0               | y          | III-4                | $0.877 \pm 0.013$ | 595                | $520 \begin{smallmatrix} +12+5 \\ -11-2 \end{smallmatrix}$                         | $0.889 \pm 0.001 \pm 0.002$         |
| 21  | GD89D              | 4.0               |            | IV-2                 | $0.877 \pm 0.013$ | 526                | $454 \begin{smallmatrix} +9+5 \\ -9-2 \end{smallmatrix}$                           | $0.884 \pm 0.001 \pm 0.002$         |
| 0   | GD91A              | 3.5               |            | I-0                  | $0.877 \pm 0.013$ | 627                | $557 \begin{smallmatrix} +10+3 \\ -11-2 \end{smallmatrix}$                         | $0.898 \pm 0.001 \pm 0.002$         |
| 25  | GD91B              | 3.5               |            | IV-6                 | $0.877 \pm 0.013$ | 650                | $578 \begin{smallmatrix} +10+5 \\ -10-2 \end{smallmatrix}$                         | $0.897 \pm 0.001 \pm 0.002$         |
| 7   | GD91C              | 4.0               | y          | I-7                  | $0.877 \pm 0.013$ | 627                | $556 \begin{smallmatrix} +11+4 \\ -11-2 \end{smallmatrix}$                         | $0.896 \pm 0.001 \pm 0.002$         |
| 33  | GD91D              | 4.5               |            | VI-3                 | $0.877 \pm 0.013$ | 693                | $615 \begin{smallmatrix} +12+5 \\ -12-2 \end{smallmatrix}$                         | $0.899 \pm 0.001 \pm 0.002$         |
| 30  | GD00A              | 2.5               | y          | VI-0                 | $0.877 \pm 0.013$ | 496                | $439 \begin{smallmatrix} +8+3 \\ -9-2 \end{smallmatrix}$                           | $0.888 \pm 0.001 \pm 0.002$         |
| 3   | GD00B              | 3.5               |            | I-3                  | $0.877 \pm 0.013$ | 697                | $613 \begin{smallmatrix} +12+5 \\ -12-2 \end{smallmatrix}$                         | $0.897 \pm 0.001 \pm 0.002$         |
| 18  | GD00C              | 3.5               | y          | III-7                | $0.877 \pm 0.013$ | 815                | $727 \begin{smallmatrix} +14+5 \\ -13-2 \end{smallmatrix}$                         | $0.903 \pm 0.001 \pm 0.002$         |
| 22  | GD00D              | 3.5               | y          | IV-3                 | $0.877 \pm 0.013$ | 813                | $723 \begin{smallmatrix} +13+5 \\ -13-2 \end{smallmatrix}$                         | $0.902 \pm 0.001 \pm 0.002$         |
| 11  | GD02A              | 2.5               | y          | III-0                | $0.877 \pm 0.013$ | 545                | $488 \begin{smallmatrix} +8+3 \\ -8-2 \end{smallmatrix}$                           | $0.893 \pm 0.001 \pm 0.002$         |
| 2   | GD02B              | 3.0               |            | I-2                  | $0.877 \pm 0.013$ | 625                | $553 \begin{smallmatrix} +10+4 \\ -10-2 \end{smallmatrix}$                         | $0.895 \pm 0.001 \pm 0.002$         |
| 31  | GD02C              | 3.5               |            | VI-1                 | $0.877 \pm 0.013$ | 788                | $700 \begin{smallmatrix} +13+5 \\ -13-2 \end{smallmatrix}$                         | $0.901 \pm 0.001 \pm 0.002$         |
| 6   | GD02D <sup>a</sup> | 4.0               | y          | I-6                  | $0.877 \pm 0.013$ | 662                | $552 \begin{smallmatrix} +11+0 \\ -11-2 \end{smallmatrix}$                         | not defined, see remark             |
| 36  | ANG1               | 4.0               |            | VI-6                 | $0.859 \pm 0.029$ | 958                | $795 \begin{smallmatrix} +43+26 \\ -43-26 \end{smallmatrix}$                       | $0.889 \pm 0.018$                   |
| 27  | ANG2               | 4.0               | y          | V-0                  | $0.866 \pm 0.025$ | 2833               | $2468 \begin{smallmatrix} +121+80 \\ -121-80 \end{smallmatrix}$                    | $0.918 \pm 0.018$                   |
| 10  | ANG3               | 3.5               | y          | II-2                 | $0.883 \pm 0.026$ | 2391               | $2070 \begin{smallmatrix} +118+60 \\ -118-67 \end{smallmatrix}$                    | $0.916 \pm 0.018$                   |
| 29  | ANG4               | 3.0               | y          | V-2                  | $0.863 \pm 0.013$ | 2372               | $2136 \begin{smallmatrix} +116+69 \\ -116-69 \end{smallmatrix}$                    | $0.916 \pm 0.018$                   |
| 8   | ANG5               | 2.5               |            | II-0                 | $0.856 \pm 0.013$ | 2746               | $2281 \begin{smallmatrix} +109+74 \\ -109-74 \end{smallmatrix}$                    | $0.918 \pm 0.018$                   |
| 9   | RG1                | 5.0               |            | II-1                 | $0.855 \pm 0.015$ | 2110               | $1908 \begin{smallmatrix} +109+62 \\ -109-62 \end{smallmatrix}$                    | $0.915 \pm 0.018$                   |
| 28  | RG2                | 4.0               |            | V-1                  | $0.855 \pm 0.015$ | 2166               | $1800 \begin{smallmatrix} +99+58 \\ -99-58 \end{smallmatrix}$                      | $0.912 \pm 0.018$                   |
| 38  | GTF32              | 3.5               | y          | VII-1                | $0.078 \pm 0.001$ | 2321               | $2251 \begin{smallmatrix} +116 \\ -116 \end{smallmatrix}$                          | $0.92 \pm 0.018$                    |
| 39  | GTF45_2            | 3.5               |            | VII-2                | $0.078 \pm 0.001$ | 2312               | 1965   | $0.92 \pm 0.018$                    |
| 37  | GTF112             | 3.5               | y          | VII-0                | $0.078 \pm 0.001$ | 2965               | 2522   | $0.92 \pm 0.018$                    |

Remarks:

<sup>a</sup> Detector GD02D does not deplete due to an unsuitable impurity concentration. The material is rather a pn junction than of p-type.



**Fig. 31** Photo of GERDA Phase II detector array, showing from left to right string 2 with three semi-coaxial detectors, and strings 3 and 4 with eight BEGe detectors, respectively. Each of the seven strings is enclosed by a transparent mini-shroud.

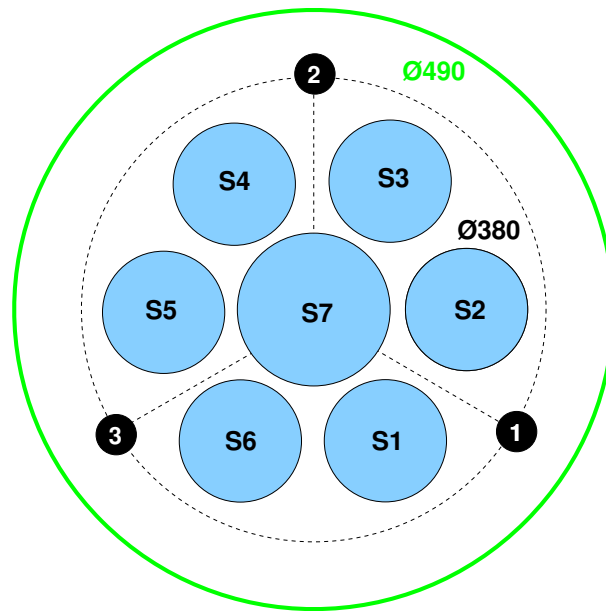


**Fig. 32** View of the array from top. The positions of the three calibration sources (1, 2, 3) and the boundaries of the LAr veto system ( $\text{Ø} 490 \text{ mm}$ ) are indicated. The surrounding radon shroud with a diameter of  $750 \text{ mm}$  [3] is not shown.

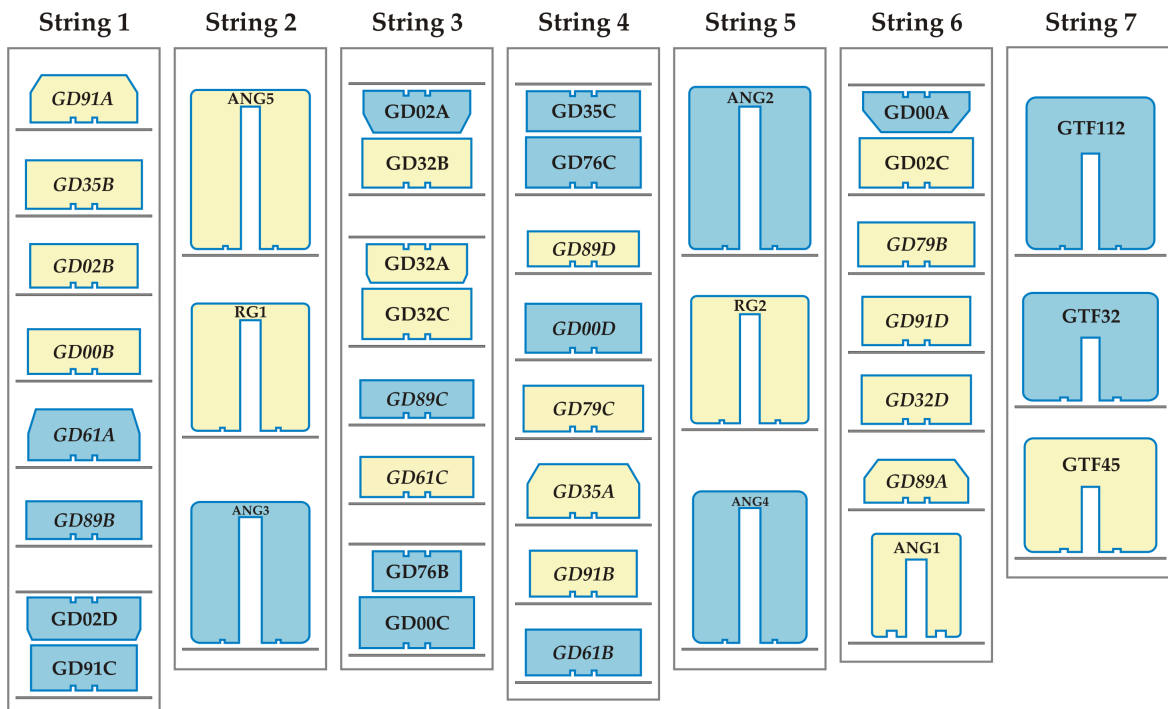


**Fig. 33** Distribution of the enriched BEGe (GDxxx) and semi-coaxial (RGx and ANGx) detectors in the various strings of the GERDA Phase II detector array; the natural low-background semi-coaxial detectors carry the labels GTFxx. Blue colored detectors carry the manufacturer's passivation on the insulating groove between the  $p^+$  and  $n^+$  contact; the yellow colored ones have this layer removed. Horizontal grey lines indicate the positions of the silicon plates (see Fig. 3). Detectors are numbered from top to bottom string by string, starting with nr. 0 in string 1 (GD91A) and ending with nr. 39 in string 7 (GTF45).

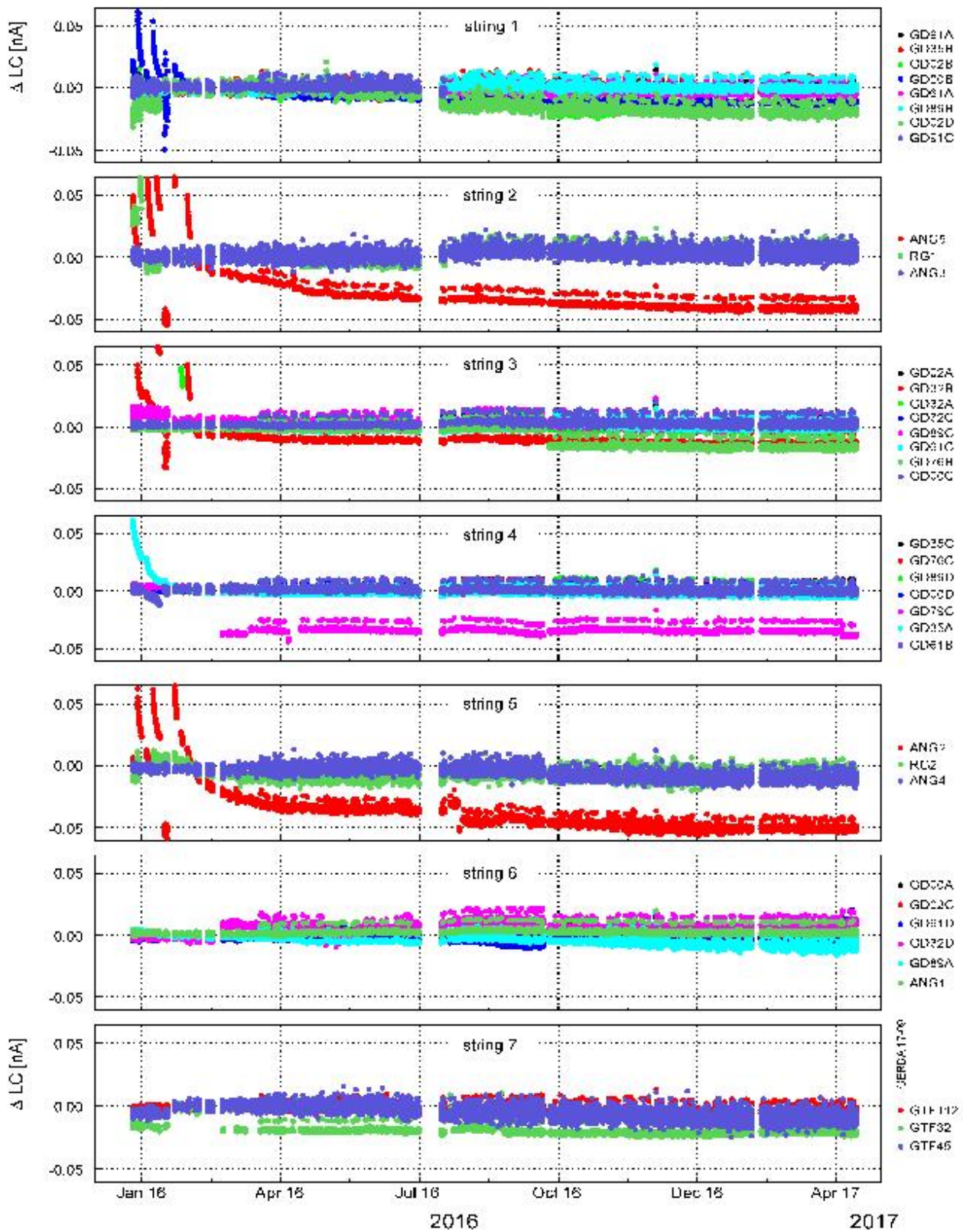


Fig. 34 Leakage currents of indicated detectors in the period from December 2015 to April 2017.